2-1-2018

Tuning the nature of defect states in black TiO2 nanostructures

Moamen Mohamed Soliman

The American University in Cairo

The Graduate School

The Nanotechnology Program

Tuning the Nature of Defect States in Black TiO_2 Nanostructures

A Thesis in
Nanotechnology
By
Moamen Mohamed Soliman

Submitted in partial fulfillment of
the requirements of the degree of
Masters of Science in Nanotechnology

August 2017

ABSTRACT

Black TiO_2 is being widely investigated due to its superior optical activity. Herein, the limitations of the hydrogenation process are unraveled by exploiting the fundamental tradeoffs affecting the overall efficiency of the water splitting process. Different reduction rates are applied to sub-100 nm TiO_2 highly efficient short nanotubes. X-ray photoelectron spectroscopy reveals changes in the stoichiometry of TiO_2 with the reduction rate. UV-Vis and Raman spectra reveal that high reduction rates promote the formation of the rutile phase in TiO_2, which is inactive towards water splitting. The electrochemical analysis discloses that low reduction rates induce higher concentration of localized electronic defect states that hinder the water splitting performance. Finally, incident photon-to-current conversion efficiency (IPCE) points out to the optimum reduction rate that attains relatively lower defects concentration as well as lower rutile content, thereby achieving the highest conversion efficiency.

The thesis of Moamen Mohamed Soliman was reviewed and approved* by the following:

Nageh K. Allam
Associate Professor,
Physics Department,
Energy of Materials Laboratory (EML),
The American University in Cairo,
Thesis Advisor,
Committee Chair.

Mohammad T. AlFiky
Assistant Professor,
Physics Department,
The American University in Cairo,
Internal Examiner.

Aiat Hegazy
Assistant Professor,
Solar Energy Department,
National Research Center,
External Examiner.

Adel M. Awad
Professor
Physics Department,
The American University in Cairo,
Moderator

*Signatures are on file in the Graduate School.

Table of Contents

List of Figures

List of Tables

Acknowledgement

Allah rendered great people to be behind me finishing this work. Dr. Nageh inspired me a lot as a role model on the personal as well as the academic side. He provided me with the knowledge and lab equipment necessary to finish this work.

Another key person who provided me with significant support is Ahmad Waleed. He has a charming, yet leadership character that gets the best out of everyone. Waleed helped me planning and finalizing this work. I would like to thank also, Menna Samir who taught me anodization 101 class, Ahmed Hamouda who was responsible for PL, Raman and UV.Vis analysis. Basamat Shaheen who did the XPS.

I hope to continue the journey of life and afterlife with my EML peers Ali, Waleed, Moustafa, Ganzoury, Hamouda, Ibrahim and Biby. They are my life friends who I knew during the last two years of my master's study.

Chapter 1: Introduction and Scope of the Thesis

1.1 Energy Demand

With the restrain in natural resources rising as a worldwide emergency, humankind is confronted with its hardest test yet. All through mankind's history, war has been the prominent answer for such natural resources conflicts. Be that as it may, advancement remained the safe house to which we regularly shielded as an asylum from undesired occasions. Subsequently, as far back as fire was found, people have grown a propensity for managing issues just as open doors for building achievements. Furnished with such learned energy, our race stays in a regularly creating state towards the more propelled, better prepared, and above all, really moral human advancements. Today, the emergency of reducing resources is most sensational in the energy business: the rest of the life-line to which people are holding, petroleum derivatives, may not be around before the finish of the 21st century.

Worldwide oil demand will increase by 7.2 million barrels per day (mb/d) in the conjecture time frame 2015-21, at a yearly average rise rate of 1.2% as detailed in table 1.1, from 94.4 mb/d in 2015, demand will hit 101.6 mb/d by 2021 [1].

Table 1.1: Global oil demand (mb/d), 2015-21 [1]

Year	*2015*	*2016*	*2017*	*2018*	*2019*	*2020*	*2021*	*15-21*
World demand (mb/d)	*94.4*	*95.6*	*96.9*	*98.2*	*99.3*	*100.5*	*101.6*	*7.2%*

On the other side of reality, the Association for the Study of Peak Oil and Gas (ASPO), utilizing a changed Klass model, anticipated the lifetime of the 2008 oil and gas reserves to be 35 and 37 years, respectively, while coal was expected to keep going for a more 107 years [2]. To

sum up, by 2112, none of the three nonrenewable energy sources would exist. This hypothesis, predicts a conceivable emergency when the new century rolled over.

Air quality concerns and worldwide climate affect constitute two noteworthy issues with our dependence on fossil fuel. Over a century back, Arrhenius explained the greenhouse effect induced by gasses, such as, CO_2 from petroleum product combustion that make the earth warm due to the rise trapping ability of infrared [3]. The relations between consuming non-renewable energy sources and environmental changes are ending up better understood [4]. The count of CO_2 has come to an extraordinary 400 ppm in 2016, it is relied upon to pass 550 ppm this century [5]. Climate models show that 550 ppm CO_2 gathering, if maintained, could in the long run outcome in an Earth-wide temperature boost practically identical in greatness (yet inverse in sign) to the worldwide cooling of the last Ice Age [5]. The results could be erratically cataclysmic and grievous as late tsunamis and hurricanes point out.

From the previously mentioned challenges the bottleneck of the energy crisis. Humankind's present reserve of fossil fuel are in effect immediately drained, leaving no stock for those will be living on this planet when earth comes up short of non-renewable energy sources. Besides, the planet's climate is being changed by people consuming fossil fuel for energy. It is, in this manner, a worldwide final offer to devise new renewable sources and additionally methods for creating energy, to end the dangerous climate change.

Hydrogen unique attributes has placed it amongst the top replacements of fossil fuel. Its global availability [6] and high mass to energy density made it more favorable than conventional non-renewable energy sources. When ignited in the presence of oxygen, one gram of hydrogen would produce triple the amount of energy produced by one gram of natural gas or crude oil [6]. Actually, hydrogen has the highest energy to mass ratio compared to alternative fuel resources [7].

Adding to that, hydrogen is 8 times lighter than methane which facilitates transport and storage [6]. Considering combustion wastes, unlike fossil fuel which produces CO_2 that contribute to greenhouse effect, the combustion of hydrogen almost produces pure water. Thus, the light gas resembles one of the best renewable energy sources.

As per current technology, the production of hydrogen gas has many routes some of which are shown in Figure 1.1. Although, 71% of our planet is water which is composed of hydrogen, the electrolysis of water to produce hydrogen constitute only 3.9% of the total hydrogen production. Such a process involves the breakdown of water molecule using electricity releasing oxygen and hydrogen. Indeed, water electrolysis has the potential to dominate hydrogen production techniques due to the great abundance of hydrogen and relatively low running cost of the process. The electricity needed for the splitting can come from sun, wind, tidal, hydro and nuclear energy sources.

The sun is a main sustainable energy source on earth. It has been radiating power of $3.9x10^{26}$ W for billions of years [8]. The nuclear fusion reaction inside the sun consumes around 637 million tons of hydrogen per second to produce 632 million tons of helium. The 5 million tons of mass defect is transformed into heat energy following the equation $E=Mc^2$ raising the surface temperature of the sun to 6000K [8]. The radiated energy gives rise to dynamic solar irradiance of variable intensity. Along these lines, an appropriate energy carrier for storage and transport of energy is required. To this end, hydrogen is believed to be a perfect energy carrier. To reduce the carbon footprint, it is suggested that the generation of hydrogen using solar energy seems to be a clean source.

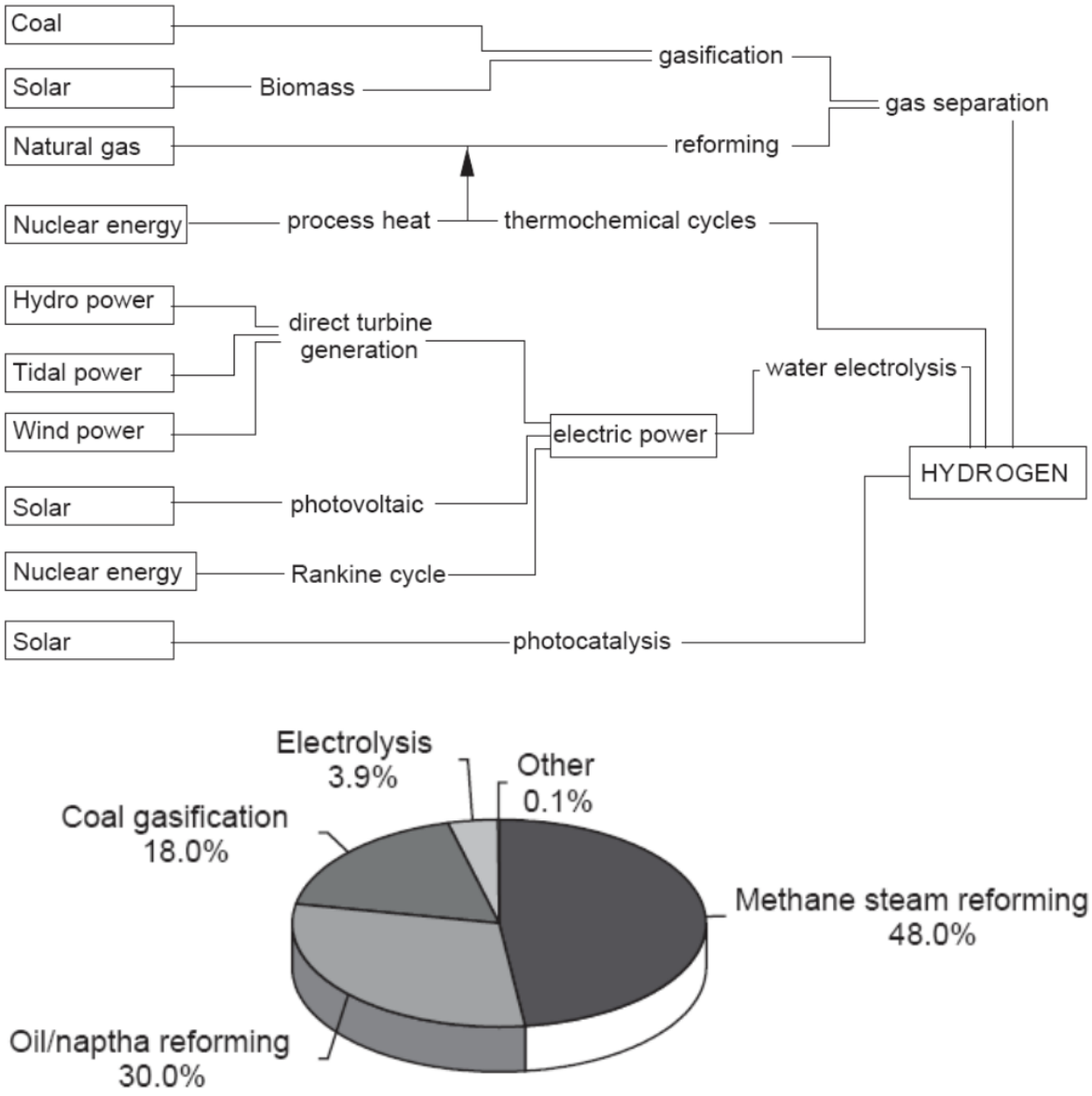

Figure 1.1: Primary energy sources and their use in hydrogen production [9].

1.2 Objectives and Scope of the Thesis

Hydrogenation has always been thought of as the process that enhances the photocatalytic activity of TiO_2 by improving light absorption and increasing carrier concentration. However, in this thesis we show that extensive hydrogenation could result in the promotion of rutile phase in TiO_2 which is inactive towards water splitting. We finally point out that there is an optimum hydrogenation rate at which the photo-conversion efficiency is maximum. The thesis will be organized as follows:

Chapter 2: Presents some background about the water splitting process as well as some criteria to evaluate efficient electrodes that include:

- Band gap matched to solar spectrum
- Band edges that favors water splitting reaction
- Facile charge dynamics

Chapter 3: Is a current literature survey of state of the art papers describing up to date contributions of different groups in black TiO_2

Chapter 4: Describes the experimental procedures followed along with the chemicals used to synthesize, anneal and characterize the nanostructures and evaluate their performance.

Chapter 5: Explains our main contribution of the thesis which is how different reduction rates for TiO_2 can be used to tune its defect nature.

Chapter 6: Concludes our work

Chapter 7: Sheds some light on future work that may further improve the photocatalytic activity of TiO_2 in water splitting process.

References

[1] IEA Secretariat, “Medium-Term Oil Market Report 2012,” *IEA Mark. Rep.*, p. 144, 2012.

[2] S. Shafiee and E. Topal, “When will fossil fuel reserves be diminished?,” *Energy Policy*, vol. 37, no. 1, pp. 181–189, 2009.

[3] S. Arrhenius, “On the Influence of Carbonic Acid in the Air upon the Temperature of the Ground,” *Philos. Mag. J. Sci.*, vol. 41, no. page 270, pp. 237–279, 1896.

[4] B. O’Neill, “Planning for Future Energy Resources,” *Science*, vol. 300, October, p. 581b–584, 2003.

[5] World Meteorological Organization, “WMO Greenhouse Gas Bulletin,” *WMO Bull.*, vol. 2015, pp. 1–4, 2015.

[6] DOE, “Alternative Fuels Data Center: Hydrogen,” *Alternative Fuels Data Center*, 2015. [Online]. Available: http://www.afdc.energy.gov/fuels/hydrogen.html. [Accessed: 06-Aug-2017].

[7] R. d. M. J.Hord and H.M.Roder, “Selected properties of Hydrogen.”, *Final report*, National Engineering Lab (NBS), Boulder, CO (USA), vol 81, pp. 211492,1981.

[8] D. T. Suzuki, A. Mason, and A. McConnell, “The sacred balance : rediscovering our place in nature, updated & expanded.” Greystone Books, 2007.

Chapter 2: Scientific Background

2.1 Water Splitting Process

Basically, the water splitting process involves the breakdown of water molecule into its initial constituents of hydrogen and oxygen using electricity in a cell of two electrodes merged in aqueous electrolyte. The cell is called photoelectrochemical cell (PEC) with at least one of the two electrodes made of semiconductor. So we end up with one of three possible electrode configurations

- Photoanode made of an n-type semiconductor and a metal cathode
- p-type semiconductor photocathode and a metal anode
- An n-type photoanode along with a p-type photocathode.

On the electronic level, the operation of n-type semiconductor PEC involves several processes within the electrodes and through the electrode/electrolyte interface (Figure 2.1) that includes [1]:

- Incident light absorbed by the semiconductor resulting in the creation of electron-hole pairs
- The holes move to the electrode/electrolyte interface oxidizing water molecules into oxygen and hydrogen ion while electrons move through the bulk of the semiconducting anode to the cathode through the external circuit.
- H^+ moves through the electrolyte from the n-type photo-anode to the metal cathode to get reduced by the externally migrating electrons.

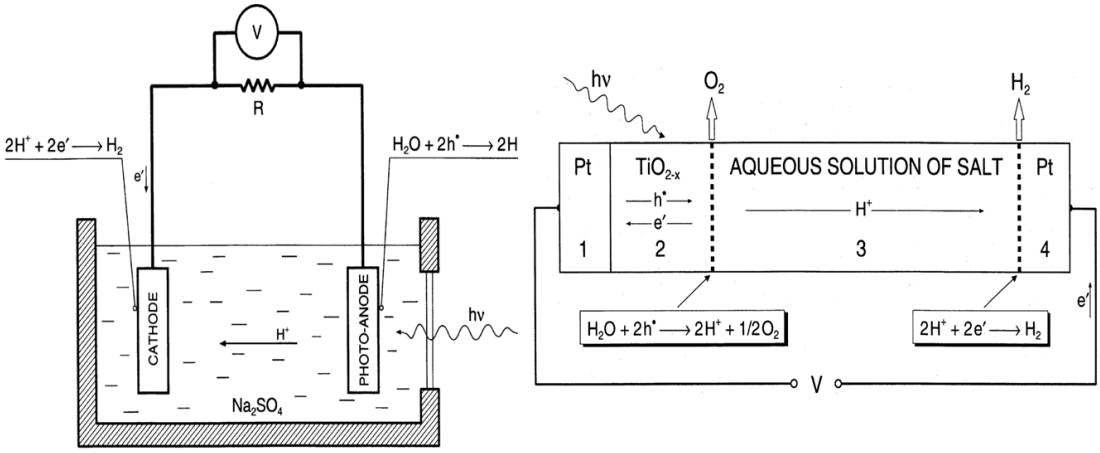

Figure 2.1*: Structure of photo-electrochemical cell for water splitting* [1].

When light falls on the photoanode, it results in the ionization of the n-type semiconductor, electrons are excited to the conduction band while holes remain at the valence band.

$$2hv \rightarrow 2e' + 2h^{\cdot} \qquad 2.1$$

where *h* is Planck's constant, *v* is the frequency of radiation, e' is the electron and $h^{\cdot}$ is the hole. An external electric field is required to prevent the recombination of those electron hole pairs. For the excitons to get separated the incident photon energy should be greater than or equal the band gap of the semiconductor. The separated electron hole pairs cause the oxidation of water molecule splitting it into oxygen and hydrogen ions.

$$2h^{\cdot} + H_2O\ (liquid) \rightarrow 2O_2\ (gas) + 2H^+ \qquad 2.2$$

The oxidation/reduction process takes place at the electrode/electrolyte interface. Simultaneously, the light-generated electrons travel through the external circuit to the cathode to reduce hydrogen ions that traveled through the electrolyte from anode to cathode.

$$2H^+ + 2e' \rightarrow H_2\ (gas) \qquad 2.3$$

Thus, the overall water splitting reaction (shown in Figure 2.1) can be written as

$$2h\nu + H_2O\ (liquid) \rightarrow 2O_2\ (gas) + H_2\ (gas) \qquad 2.4$$

This reaction can only take place if the energy of the absorbed photon is greater than or equal the threshold energy E_t. The water splitting reaction energy is given by:

$$E_i = \frac{\Delta G^o_{(H2O)}}{2N_A} \qquad 2.5$$

where $\Delta G^o_{(H2O)}$ is the standard free enthalpy per mole of the water splitting reaction which is 237.141 kJ/mol and N_A is Avogadro's number equal to 6.022×10^{23} mol^{-1}. Thus, the water splitting reaction energy is 1.23 eV, which must be provided by light or external bias in order for the reaction to take place.

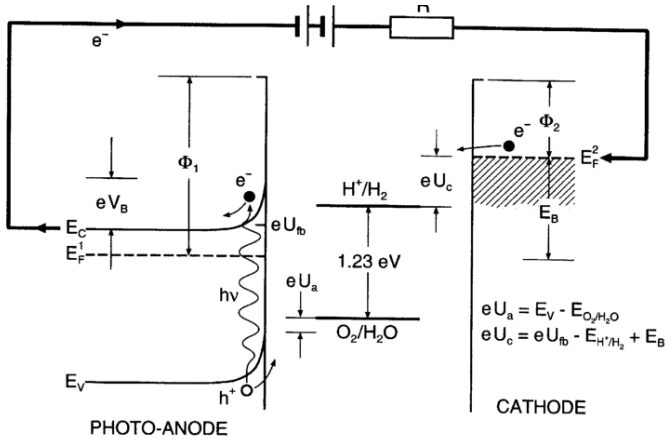

Figure 2.2: Schematic diagram of PEC presenting the dynamics of water splitting reaction [1]

2.2 Electrode Characteristics

For the water splitting reaction to take place, the n-type photo-anode must satisfy some criteria that include [2]:

- Band Gap Width: The semiconductor band gap must be matched to absorb most of the solar spectrum [3].
- Band Edge Positions: The valence band minimum and the conduction band maximum must straddle the water redox potential.
- Stability of the Electrodes: The free enthalpies of oxidation and reduction must be matched to the valence band maximum and conduction band minimum, to prevent photocorrosion.
- Charge Carrier Dynamics: The electrode structure must allow for efficient charge separation.

2.2.1 Band Gap Width

The band gap of the semiconductor must be matched to absorb solar radiation of which 60% are concentrated around wavelengths of 400nm to 700nm. The solar energy can be written in terms of wavelength as

$$E = \frac{hc}{\lambda} \qquad 2.6$$

where c is the speed of light and λ is the wavelength. Thus, it might be energy efficient to use a semiconductor with a band gap energy E_g in range of $1.7\ eV < E_g < 3.1\ eV$ such that most of the solar radiation energy is utilized.

2.2.2 Band Edge Position

Along with the matched band gap of the semiconductor to solar spectrum comes an equally important criterion, that the semiconducting electrode should satisfy is the straddling of its band gap with water reduction and oxidation potentials. Figure 2.3 shows the positions of the valence band maximum and the conduction band minimum of different semiconductors along with the water oxidation and reduction potentials versus the normal hydrogen electrode (NHE) reference. In order for the water splitting reaction to take place, the water redox potentials should fall inside the band gap of the semiconductor. In other words, the valence band maximum of the semiconductor should be lower (more anodic) that the oxidation potential of water such that facile diffusion of holes from the semiconductor to the electrolyte can take place resulting in the splitting of water. Adding to that, the semiconductor conduction band minimum should be greater (more cathodic) than the reduction potential of hydrogen ions such that the externally migrated electrons in the PEC would favor to reduce the hydrogen collected at the cathode.

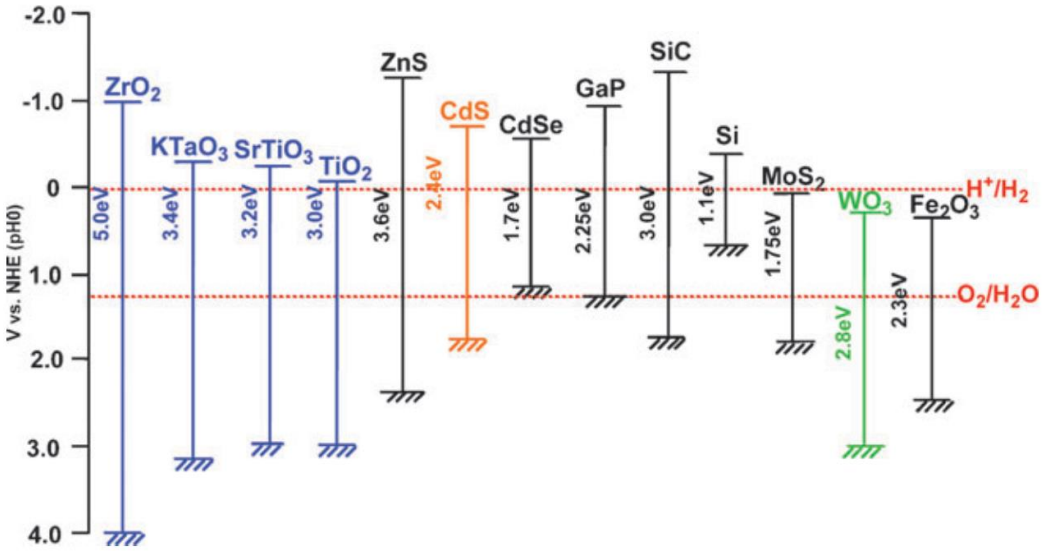

Figure 2.3: Water redox potentials shown relative to the band gaps of different semiconductors [3]

For the semiconductor to be stable in the electrolyte under illumination, the light induced electron hole pairs should favor to oxidize water and reduce hydrogen in the electrolyte rather than oxidizing the semiconductor itself causing its decomposition. Gerischer [4] suggested a quantitative metric that can be used to test the stability of the semiconductor as shown in Figure 2.4. The oxidation and reduction free enthalpies of the semiconductor namely $E_{p,d}$ and $E_{n,d}$ should be straddling with the water oxidation and reduction potentials.

- The oxidation potential of water should be lower (more anodic) than $E_{p,d}$
- The reduction potential of hydrogen should be greater (more cathodic) than $E_{n,d}$

Such that the generated carriers would favor to interact with the electrolyte rather than decomposing the electrodes.

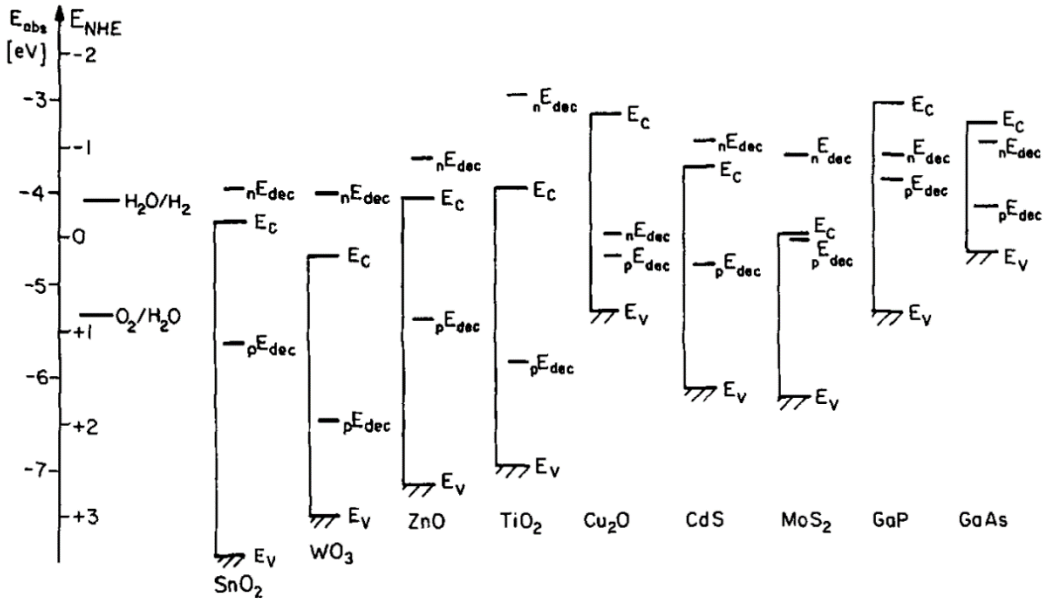

Figure 2.4: Decomposition potentials of different semiconductors drawn relative to water redox potentials [4].

2.2.3 Charge Carrier Dynamics

After the generation of electron hole pairs in the semiconductor photo-anode with the aid of light, the opposite charges should migrate in different directions. Holes are required to migrate to the anode/electrolyte interface to oxidize water while electrons are required to migrate to the cathode/electrolyte interface to reduce hydrogen. However, there are some factors that may result in the trapping of charge carriers preventing them from reaching the electrolyte through different electrodes. These factors include [5]:

- Bulk defects such as vacancies, interstitials, and grain boundaries that result in defect states that which trap the electrons.
- Trap states that lie on the surface, due to dangling bonds, or adsorbed electrolyte species that act as electron sinks.

Thus, electrons and holes have limited mobility inside the semiconductor before recombination will eventually take place. The average distance a charge carrier can move inside the electrolyte before recombining is called Debye diffusion length [6] and is given by:

$$\lambda_D = \left(\frac{KT\varepsilon\varepsilon_r}{N_D e^2}\right)^{1/2} \qquad 2.7$$

where K is Boltzman constant, T is the material temperature, ε is the permittivity of free space, ε_r is the relative permittivity of the material, N_D is the carrier concentration and finally e is the electronic charge.

References

[1] T. Bak, J. Nowotny, M. Rekas, and C. Sorrell, "Photo-electrochemical hydrogen generation from water using solar energy. Materials-related aspects," *Int. J. Hydrogen Energy*, vol. 27, no. 10, pp. 991–1022, 2002.

[2] B. S. Shaheen, H. G. Salem, M. A. El-sayed, and N. K. Allam, "Thermal / Electrochemical Growth and Characterization of One-Dimensional ZnO/TiO_2 Hybrid Nanoelectrodes for Solar Fuel Production," *J. Phys. Chem. C*, Vol *117* (36), pp 18502–18509, 2013.

[3] T. Minemoto, Y. Nakada, H. Takahashi, and H. Takakura, "Uniqueness verification of solar spectrum index of average photon energy for evaluating outdoor performance of photovoltaic modules," *Sol. Energy*, vol. 83, no. 8, pp. 1294–1299, 2009.

[4] H. Gerischer, "4. Solar Photoelectrolysis with Semiconductor Electrodes." , Solar Energy Conversion, pp. 115-172, 1979

[5] N. K. Allam, "An investigation into the doping and crystallinity of anodically fabricated TiO_2 nanotube arrays: Towards an efficient material for solar energy applications," *PhD thesis*, The Pennsylvania State University, 2009.

[6] G. Hautier, A. Miglio, G. Ceder, G.-M. Rignanese, and X. Gonze, "Identification and design principles of low hole effective mass p-type transparent conducting oxides.," *Nat. Commun.*, vol. 4, p. 2292, 2013.

Chapter 3: Literature Survey

3.1 Straddling and Stability

As shown in Figures 3.1 and 3.2, the band gap of TiO_2 straddles with the water oxidation and reduction potentials which suggests that TiO_2 might be a suitable candidate for water splitting as its band gap is 3.1 eV, which could easily energize the water splitting reaction. What makes TiO_2 more promising is its high stability. It fulfills the stability requirements by having oxidation and reduction free enthalpies that straddle with water redox potentials.

3.2 Improving Charge Dynamics

With the advancement of high-precision structural and spectroscopic characterization tools, the ability to accurately control the structure of nanomaterials has been enabled. Amongst the markets most benefited by these capabilities is that of nanostructured photocatalysis, where the large surface area-to-volume ratio maximizes the number of active sites onto which reactions may take place [1]. Consequently, efforts to create thinner films, [2] smaller nanoparticles, and shorter nanotubes [3], [4] for photocatalytic applications, such as photoelectrochemical cells, have boosted in the past couple of years. Such endeavors pave the way towards developing the most efficient photocatalyst structures. Structure, however, is not the only variable in the question of efficient photocatalysis, optical and electronic properties are as critical. With TiO_2 being one of the most-studied photocatalysts for water splitting, [5] researchers have been attempting to get the most out of this relatively-cheap catalyst [6]. Today, after more than 45 years of development, efforts still show promise in TiO_2 photocatalysis.

To this end, our group has recently devised a one-step synthesis route to one-dimensional (1D), sub-100 nm TiO_2 nanostructures, which have demonstrated higher efficiencies compared to regular, long TiO_2 nanotubes [7]. Such enhancement was attributed to the decrease in electron pathway, leading to optimized charge collection.

3.3 Reducing the Band Gap

Our optimized structures, however, still face the ever-challenging optical absorption deficiency of the wide band gap semiconductor. That being said, annealing under different atmospheres has proven to be one of the cheapest routes towards adjustment of electronic properties [8]. In particular, H_2-annealing has seen special attention owing to promising traits of the resulting black TiO_2 [9]–[17]. Studies have reported visible light absorption, [18] increased charge carrier density, [19] and enhanced charge separation in the UV region [13]. Experimentally, electron paramagnetic resonance (EPR) studies throughout the literature [9]–[11], [20] proved the presence of Ti^{3+} in the bulk of black TiO_2. Those Ti^{3+} states were thought to be the reason behind the observed enhancements, where a defect band is created below the CBM, increasing electron density and effectively reducing the optical band gap of TiO_2 [12], [21]–[23]. Other studies [16], [17], [24] attributed the visible light-absorption to the effective rise of the valence band minimum (VBM) *via* the incorporation of hydrogen states above the O 2p VBM. On the theoretical side, density functional theory (DFT) calculations confirmed both views [9], [25]–[33] However, numerous DFT studies infer that the nature of the created defect states may not always make them beneficial.[13] Ling et al. [12] reported the creation of deep trap states, that are localized in real space, within the band gap of black TiO_2 as a result of H_2-annealing. Confirming Ling's conclusions, *Ataei* et al. [34] presented a relation between that phenomenon and the

position of the hydrogen atom inside the lattice of TiO_2. On the scale of lab experiments, however, these observations are yet to be confirmed.

Indeed, the difference between deep and shallow defect states has been suggested to lie within the so-called cross-section of the defect inside the lattice [35]. Roughly, a cross-section greater than 10^{-15} cm^2 would be strongly attractive to electrons passing by towards the CBM. The effective radius of a defect (r_d) has been suggested to follow the relation [36]:

$$r_d = \frac{zq^2}{\varepsilon k_B T} \qquad 3.1$$

where q and z are the electron and defect charges, respectively. Trap states may take cross-sections up to 10^{-9} cm^2, making them strongly attractive to electrons. Effectively, being delocalized in reciprocal space, such states can 'capture' carriers with different values of momenta, increasing the probability of trapping, compared to shallow defect states that may only take up certain values of momenta in reciprocal space [35]. Throughout the following discussion, the real space notation would be used instead: localized for deep trap states, and delocalized for shallow donor states. To the authors' best knowledge, a discussion of both natures of defect states within the framework of black TiO_2 is lacking in literature. Indeed, a synthesis route that proves to be selective when it comes to both types of defect states would be critical if black TiO_2 catalysts are to be used on an industrial scale.

3.4 Disordered Surface Structure:

The chemical, atomic and electronic structure of disordered shell was studied in black TiO_2 by Tian et al. [37] using advanced transmission electron microscopy methods. Figure 3.1 presents the crystal structure of hydrogenated TiO_2 which is comprised of three parts namely: outer shell,

transition region and bulk core. The outer shell is composed of disordered Ti_2O_3 while the transition region is composed of four to five monolayers of defective rutile phase (marked by dashed rectangle in Figure 3.1) containing Ti interstitials (marked by arrows). Then covered by interstitial Ti atoms (white rectangle), which is finally connected to the pure rutile core.

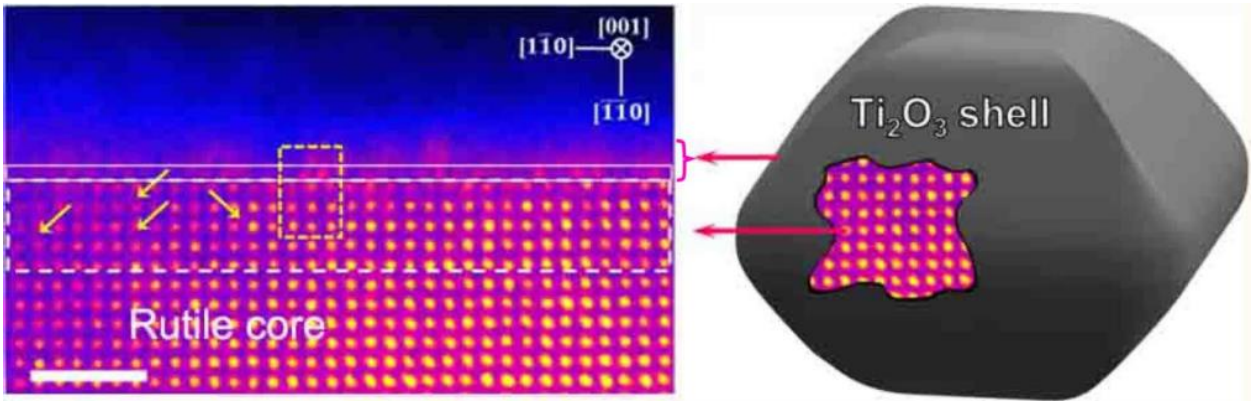

Figure 3.1: High-angle annular dark-field image (left) and schematic of the black TiO_2 surface (right).

3.5 Ti^{3+} and Oxygen Vacancies

Different characterization techniques have been used to prove the existence of Ti^{3+} and oxygen vacancies in black TiO_2. X-ray photoelectron spectroscopy, electron paramagnetic resonance and Raman spectroscopy were used to characterize TiO_2 prepared by different methods [38]–[42]. Lie et al [43] used TiH_2 and H_2O_2 as precursors to synthesize TiO_{2-x} using ion diffusion reaction. Their XPS data showed peaks of Ti 2p3/2 (457.4 ev) and Ti 2p1/2 (463.2 ev) located at lower binding energies, indicating the existence of Ti^{3+} in the black TiO_2 nanoparticles. Wang et al [44] prepared black TiO_2 by calcining at 440 ^oC pristine TiO_2 under 10 bar H_2 atmosphere for 2 hours. The Raman spectra showed peaks that were shifted to higher frequencies than normal TiO_2 implying the formation of oxygen vacancies by hydrogen treatment. Grabstanowicz et al. [45] also

oxidized TiH_2 in H_2O_2 followed by Argon annealing at 630 ^{O}C then used electron paramagnetic resonance to prove the existence of Ti^{3+} in black TiO_2.

3.6 Ti-OH and Ti-H Groups

Ti-OH and Ti-H groups were often found in hydrogenated TiO_2 nanostructures [13], [17], [46]–[48]. Chen et al. [17] reported a shoulder peak in the O 1s XPS core spectra which was attributed to Ti-OH. Similar studies have also revealed the same results for nanotubes [49] and nanowires [13]. Also, Wang et al. [10] characterized Ti-OH groups using Fourier Transform Infrared Spectra. Several peaks were observed at 3710, 3685, 3670 and 3645 cm-1. The first peak corresponds to terminal OH group while the last three correspond vacancies. The presence of Ti-OH groups was confirmed using 1H nuclear magnetic resonance (NMR) spectra.

3.7 Optical Absorption

Chen et al. [17] found that the optical band gap of TiO_2 was significantly narrowed by hydrogenation resulting in a red shift in the absorption spectra to 1200 nm which corresponds to 1.0 eV band gap. It was also shown that the valence band maximum was blue shifted towards the vacuum level. Thus, the optical transition from the raised valence band to the conduction band tails induced structural disorders is responsible for the band gap narrowing. Other groups have also reported similar shifts in the band gap [9], [11], [24], [50]. Fan et la. [51] demonstrated that hydroxyl groups reduce the band gap of black TiO_2 by inducing localized band bending. Furthermore, Liu et al. [22] revealed that oxygen vacancies and Ti^{3+} induce defect states that are responsible for visible light absorption. Tian et al. [52] used pulsed laser vaporization to prepare black TiO_2 that exhibited visible light absorption.

3.8 Theoretical Calculation

It is widely known that hydrogenation of TiO_2 introduce shallow defect states in the band gap that result in enhanced optical activity [9], [11], [17], [24],[53]. Chen et al. [17] demonstrated that when hydrogen atoms were bonded to O and Ti, two band gap states appear at about 1.8 and 3.0 eV. The higher energy group resulted from the interaction of H 1s with Ti 3d, while the lower energy group resulted from the interaction of H 1s hybridized with hybridized O 2p and Ti 3d orbitals. Raghunath et al. [54] revealed that mid gap state at 1.2 eV below the conduction band minimum existed as a result of interaction of H 1s with Ti 3d. Those H atoms acted as electro donors leading to the shift of fermi level of TiO_2 towards the conduction band. Also, Deng et al. [32] showed the formation of states at 0.7 eV above the valence band minimum as a result of Ti-H bond. While Pan et al. [8] demonstrated that substitutional hydrogen reduces the band gap of rutile and brookite and interstitial narrows the band gap of anatase, rutile and brookite. DFT calculations also revealed that hydrogenation induces lattice disorder to the surface of nanophase anatase which contributes to mid band gap states[55]. Chen et al. [56] compared two large TiO_2 clusters $Ti_{210}O_{420}H_{12}$ representing white TiO_2 nanocrystal and $Ti_{218}O_{436}H_{70}$ as black TiO_2. The black TiO_2 showed band gap states extending from the valence band maximum to 1.2 ev above the valence band. Also, mid band gap states have been observed at about 1.8 ev above the valence band maximum. Liu et al. [14] showed that distortion in the Ti sublattice results in red shift in the conduction band minimum and blue shift to the valence band maximum. While O sublattice distortion only leads to blue shift to the valence band maximum. Taking that in to consideration, there are more Ti-O bond fixed with Ti more than O, more energy is required to distort the Ti sublattice than O sublattice. Therefore, O sublattice disorder is more likely to take place, which is in line with experimental observation that hydrogenation raises the valence band maximum.

3.9 Charge Carrier Transfer Property

The improved photocatalytic activity of black TiO_2 has been widely attributed to increased donor density [13], [53] introduced oxygen vacancies [11], [57] and disordered surface layer [14], [17], [58]. Wang et al. [13] demonstrated that black TiO_2 has donor density higher than white TiO_2 by 4 orders of magnitude which was attributed to the higher concentration of oxygen vacancies which acts as electron donors in n-type TiO_2. The greater donor density improves the charge transport in TiO_2. Jiang et al. suggested that oxygen vacancies could act as electron traps that improve charge separation and significantly reduce recombination [38]. They found that black TiO_2 has lower photoluminance emission intensity than white TiO_2 by one third which indicates lower recombination rate for black TiO_2 due to higher concentration of oxygen vacancies. Yan et al. [59] reported the disordered surface layer of black TiO_2 improves charge separation and suppress its recombination at the electrode electrolyte interface.

3.10 Black TiO_2 review

Pan et al. [8] investigated the effect of hydrogen doping on TiO_2 using theoretical DFT calculations. They revealed that the effect of hydrogen doping is phase dependent. As for interstitial hydrogen, the band gaps were 2.81, 2.79, and 2.39 eV for anatase, brookite and rutile, respectively (Figure 3.2 b) while their calculated intrinsic band gaps are 2.96, 2.91 and 2.52 eV, respectively (Figure 3.2 a). However, for interstitial hydrogen only brookite and rutile show narrowed band gaps of 2.59 and 2.24 eV (Figure 3.2 c). Also, a shift in the Fermi level in both cases take place due to the electron contributed by the hydrogen atoms which is greatly delocalized.

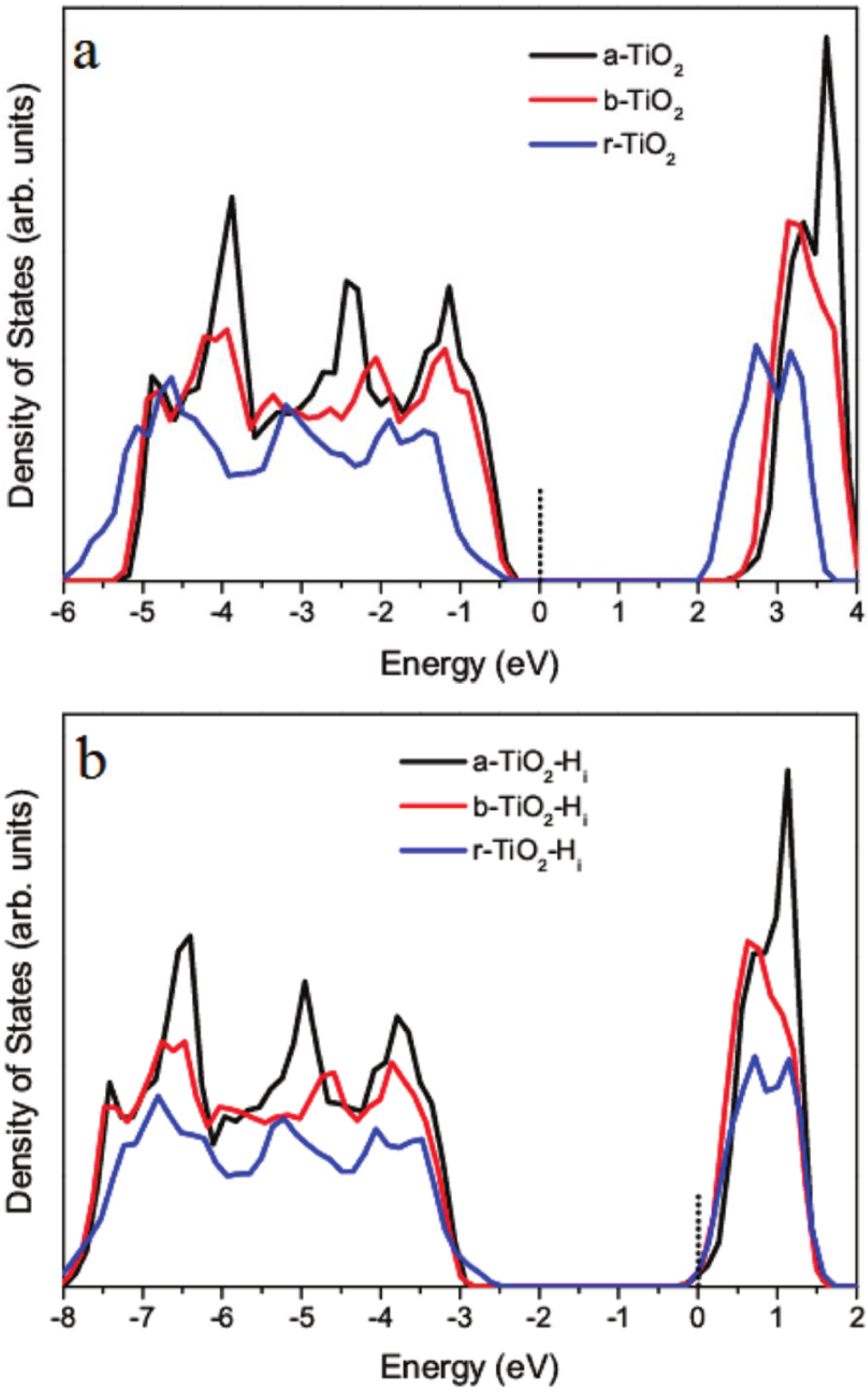
a
a-TiO2
b-TiO2
r-TiO2
Density of States (arb. units)
-6 -5 -4 -3 -2 -1 0 1 2 3 4
Energy (eV)
b
a-TiO2-Hi
b-TiO2-Hi
r-TiO2-Hi
Density of States (arb. units)
-8 -7 -6 -5 -4 -3 -2 -1 0 1 2
Energy (eV)

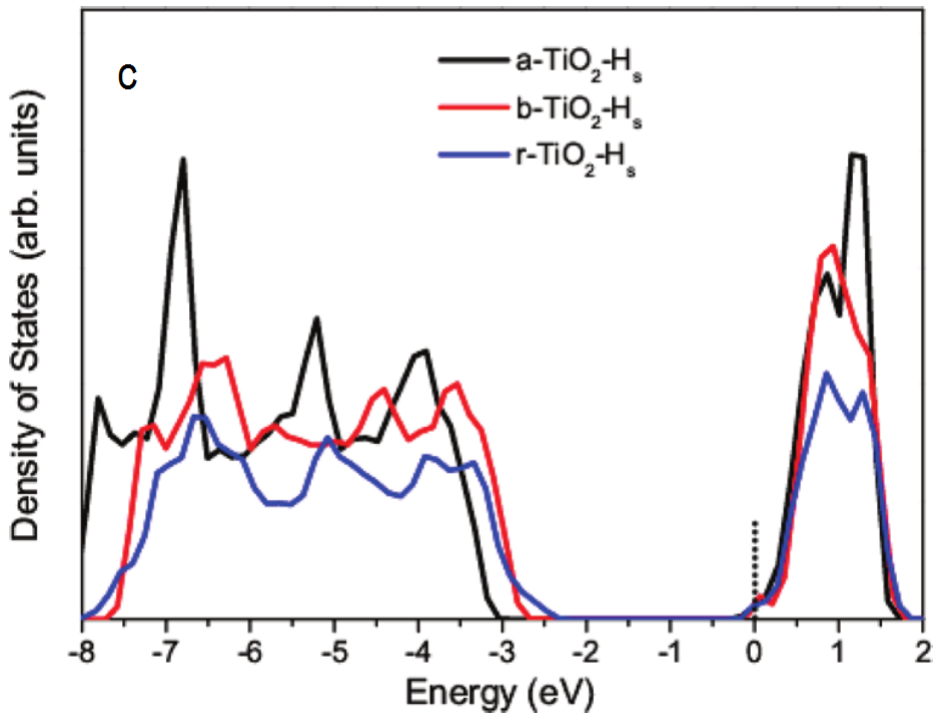

Figure 3.2: Full density of states of the three polymorphs of TiO_2 anatase, brookite and rutile for (a) intrinsic, (b) interstitial and (c) substitutional hydrogen[8].

Damon et al. [12] used time-resolved fluorescence to investigate ultrafast relaxation dynamics of hydrogenated TiO_2. They illuminated TiO_2 samples with ultraviolet and visible light and summarized their findings in Figure 3.3.

- There is an intrinsic defect state located at 0.3 eV below the conduction band minimum of TiO_2.
- Oxygen vacancies create defect states located at 0.75 eV below the conduction band minimum of TiO_2.
- Hydrogen treatment introduces nonflorescent mid-band gap states located below the oxygen vacancy level.
- Naldoni et al. [24] domenstrated experimentally that black TiO_2 has a narrowed band gap of 1.85 eV due to valence band tailing as a result surface disorder created by hydrogen

treatment which also induces oxygen vacancies as shown in Figure 3.4. Such vacancies are located at 0.7-1.0 eV below the conduction band minimum. The authors also attributed the black color of hydrogenated TiO_2 to the transitions between the valence band tail and the oxygen vacancy defect state. Finally, it was revealed that there are no defect states in the band gap introduced by hydrogen bonding with TiO_2 as shown in Figure 3.4.

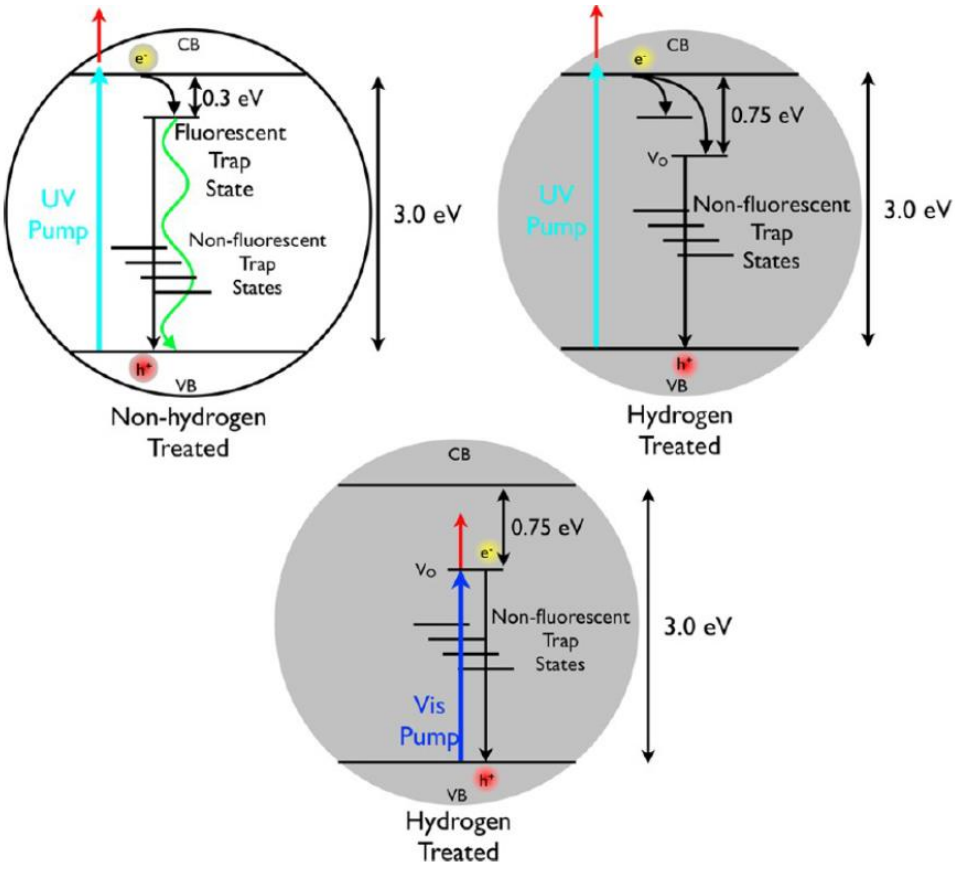

Figure 3.3: Proposed energy band diagram for black TiO_2 [12].

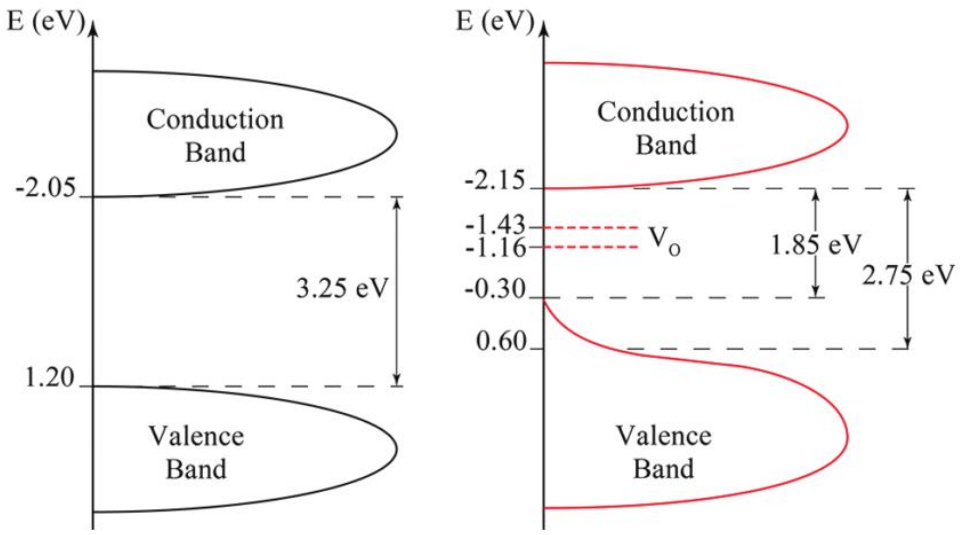

Figure 3.4: Proposed energy band diagram model for hydrogenated TiO_2 [24].

Wang et al. [13] studied hydrogenated TiO_2 at different temperatures. They revealed that as the hydrogenation temperature increases the incident photon to current conversion efficiency degrades as shown in Figure 3.5 a. Also, some important facts regarding how hydrogenation affects the band structure of hydrogenated TiO_2 include:

- Ti-OH groups form energy states at 0.7-2.6 eV below the valence band minimum as shown in Figure, which should not lead to visible light absorption as shown in Figure 3.5 b.
- Oxygen vacancies induce mid band gap states 0.7-1.0 eV below the conduction band minimum.
- Hydrogen treatment promote oxygen vacancies which increases the donor density in TiO_2

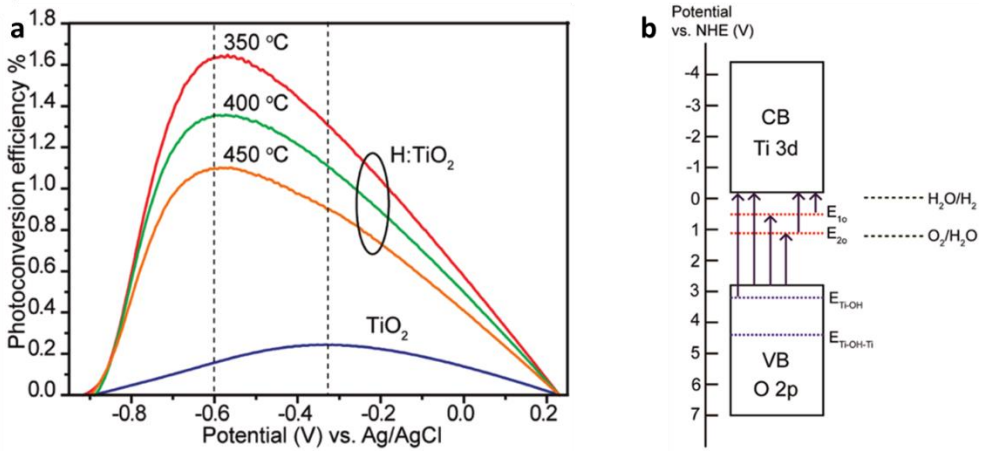

Figure 3.5:(a) IPCE of TiO_2 treated at different temperatures, and (b) proposed energy band diagram of hydrogen treated TiO_2 [13].

Wang et al. [10] revealed that hydrogenation induces band gap defects located at 0.92 − 1.37 eV below the conduction band minimum as shown in Figure 3.6 a. Adding to that, band tailing was observed at the conduction band minimum which reduces the band gap by 0.8 eV as shown in Figure 3.6 b. The electronic transitions between valence band, intermediate band gap states and conduction band tail have allowed the absorption of UV, visible and IR light.

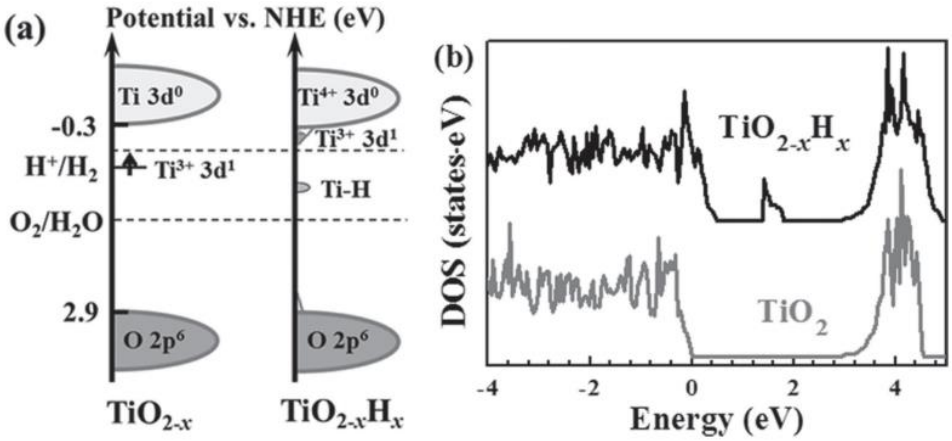

Figure 3.6: (a) Energy band diagram model (b) Density of states of white and black TiO_2 [10].

Kang et al. [11] revealed that hydrogenation process induces valence band tailing which reduces the band gap by 0.5 eV as depicted in Figure 3.7. However, hydrogenation doesn't affect the conduction band. Also, conventional mid band gap defect states at 0.75-1.18 eV were also reported.

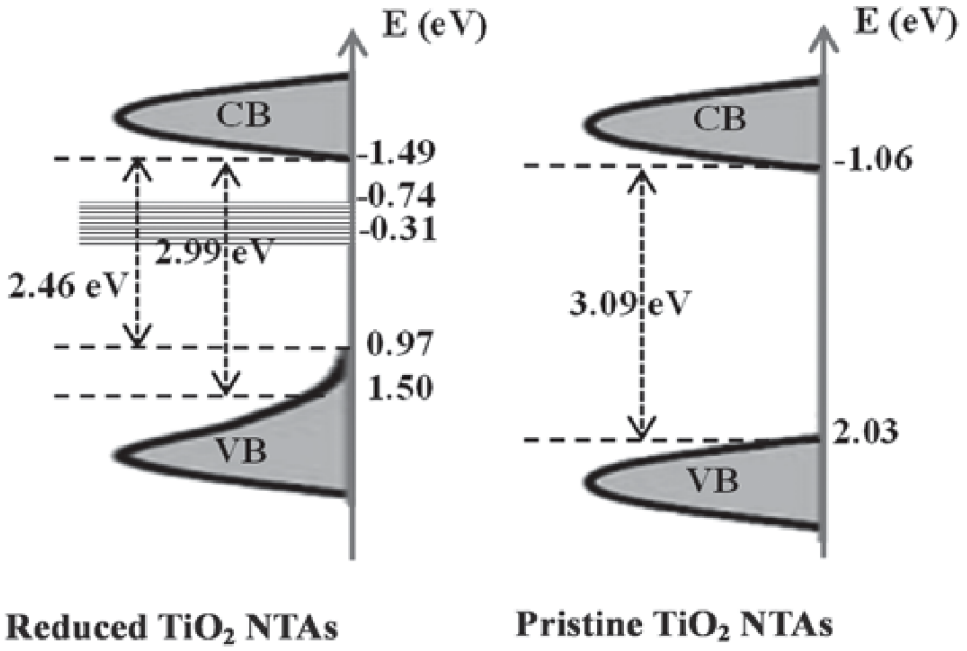

Figure 3.7: Energy band gap diagram of reduced TiO_2 Vs. white TiO_2 [11].

References

[1] E. Roduner, “Size matters: why nanomaterials are different,” *Chem. Soc. Rev.*, vol. 35, no. 7, p. 583, 2006.

[2] D. G. Schlom, L. Q. Chen, X. Pan, A. Schmehl, and M. A. Zurbuchen, “A thin film approach to engineering functionality into oxides,” *J. Am. Ceram. Soc.*, vol. 91, no. 8, pp. 2429–2454, 2008.

[3] Y. Liu, B. Zhou, J. Li, X. Gan, J. Bai, and W. Cai, “Preparation of short, robust and highly ordered TiO_2 nanotube arrays and their applications as electrode,” *Appl. Catal. B Environ.*, vol. 92, no. 3–4, pp. 326–332, 2009.

[4] X. Gao *et al.*, “Enhanced photovoltaic performance of perovskite $CH_3NH_3PbI_3$ solar cells with freestanding TiO_2 nanotube array films.,” *Chem. Commun. (Camb).*, vol. 50, no. 48, pp. 6368–71, 2014.

[5] X. Chen and S. S. Mao, “Titanium dioxide nanomaterials: Synthesis, properties, modifications and applications,” *Chem. Rev.*, vol. 107, no. 7, pp. 2891–2959, 2007.

[6] K. Hashimoto, H. Irie, and A. Fujishima, “A Historical Overview and Future Prospects,” *AAPPS Bull.*, vol. 17, no. 6, pp. 12–28, 2007.

[7] M. Samir, M. Salama, and N. K. Allam, “Sub-100 nm TiO_2 tubular architectures for efficient solar energy conversion,” *J. Mater. Chem. A*, vol. 4, no. 24, pp. 9375–9380, 2016.

[8] H. Pan, Y. Zhang, V. B. Shenoy, and H. Gao, “Effects of H- , N- , and (H , N) -Doping on the Photocatalytic Activity of TiO 2,” J. Phys. Chem. C, vol. 115, pp. 12224–12231, 2011.

[9] M. M. Khan *et al.*, “Band gap engineered TiO_2 nanoparticles for visible light induced

photoelectrochemical and photocatalytic studies," *J. Mater. Chem. A*, vol. 2, no. 3, pp. 637–644, 2014.

[10] Z. Wang *et al.*, "H-doped black titania with very high solar absorption and excellent photocatalysis enhanced by localized surface plasmon resonance," *Adv. Funct. Mater.*, vol. 23, no. 43, pp. 5444–5450, 2013.

[11] Q. Kang, J. Cao, Y. Zhang, L. Liu, H. Xu, and J. Ye, "Reduced TiO_2 nanotube arrays for photoelectrochemical water splitting," *J. Mater. Chem. A*, vol. 1, no. 18, p. 5766, 2013.

[12] D. A. Wheeler *et al.*, "Probing the nature of bandgap states in hydrogen-treated TiO_2 nanowires," *J. Phys. Chem. C*, vol. 117, no. 50, pp. 26821–26830, 2013.

[13] G. Wang *et al.*, "Hydrogen-treated TiO_2 nanowire arrays for photoelectrochemical water splitting," *Nano Lett.*, vol. 11, no. 7, pp. 3026–3033, 2011.

[14] L. Liu, P. Y. Yu, X. Chen, S. S. Mao, and D. Z. Shen, "Hydrogenation and disorder in engineered black TiO2," *Phys. Rev. Lett.*, vol. 111, no. 6, pp. 1–5, 2013.

[15] Y. H. Hu, "A highly efficient photocatalyst-hydrogenated black TiO_2 for the photocatalytic splitting of water," *Angew. Chemie - Int. Ed.*, vol. 51, no. 50, pp. 12410–12412, 2012.

[16] X. Chen *et al.*, "Properties of disorder-engineered black titanium dioxide nanoparticles through hydrogenation.," *Sci. Rep.*, vol. 3, pp. 1510-1-1510–7, 2013.

[17] X. Chen, L. Liu, P. Y. Yu, and S. S. Mao, "Increasing solar absorption for photocatalysis with black hydrogenated titanium dioxide nanocrystals.," *Science*, vol. 331, no. 6018, pp. 746–50, 2011.

[18] R. Asahi, T. Morikawa, T. Ohwaki, and Y. Taga, "Visible-Light Photocatalysis in Nitrogen-

Doped Titanium Oxides," *Science* vol. 293, no. 5528, pp. 269–271, 2001.

[19] G. Wang *et al.*, "Supporting Information Hydrogen-Treated TiO_2 Nanowire Arrays for Photoelectrochemical Water Splitting," *Nano Lett.*, vol. 11, no. 7, pp. 1–10, 2011.

[20] R. F. Howe and M. Gratzel, "EPR Observation of Trapped Electrons In Colloidal TiO_2," *J. Phys. Chem.*, vol. 89, no. 21, pp. 4495–4499, 1985.

[21] B. Li, Z. Zhao, Q. Zhou, B. Meng, X. Meng, and J. Qiu, "Highly efficient low-temperature plasma-assisted modification of TiO_2 nanosheets with exposed {001} facets for enhanced visible-light photocatalytic activity," *Chem. - A Eur. J.*, vol. 20, no. 45, pp. 14763–14770, 2014.

[22] L. Liu *et al.*, "Engineering Coexposed {001} and {101} Facets in Oxygen-Deficient TiO_2 Nanocrystals for Enhanced CO_2 Photoreduction under Visible Light," *ACS Catal.*, vol. 6, no. 2, pp. 1097–1108, 2016.

[23] S. Hoang, S. P. Berglund, N. T. Hahn, A. J. Bard, and C. B. Mullins, "Enhancing visible light photo-oxidation of water with TiO_2 nanowire arrays via cotreatment with H_2 and NH_3: synergistic effects between Ti^{3+} and N.," *J. Am. Chem. Soc.*, vol. 134, no. 8, pp. 3659–62, 2012.

[24] A. Naldoni *et al.*, "Effect of nature and location of defects on bandgap narrowing in black TiO_2 nanoparticles," *J. Am. Chem. Soc.*, vol. 134, no. 18, pp. 7600–7603, 2012.

[25] J. Stausholm-Møller, H. H. Kristoffersen, B. Hinnemann, G. K. H. Madsen, and B. Hammer, "DFT+U study of defects in bulk rutile TiO_2," *J. Chem. Phys.*, vol. 133, no. 14, 2010.

[26] M. V. Koudriachova, S. W. de Leeuw, and N. M. Harrison, “First-principles study of H intercalation in rutile TiO_2,” *Phys. Rev. B*, vol. 70, no. 16, p. 165421, 2004.

[27] C. Di Valentin, G. Pacchioni, and A. Selloni, “Electronic structure of defect states in hydroxylated and reduced rutile TiO_2(110) surfaces,” *Phys. Rev. Lett.*, vol. 97, no. 16, p. 166803 - 166807, 2006.

[28] S. Na-Phattalung *et al.*, “First-principles study of native defects in anatase TiO_2,” *Phys. Rev. B - Condens. Matter Mater. Phys.*, vol. 73, no. 12, pp. 1–6, 2006.

[29] A. Amore Bonapasta, F. Filippone, G. Mattioli, and P. Alippi, “Oxygen vacancies and OH species in rutile and anatase TiO_2 polymorphs,” *Catal. Today*, vol. 144, no. 1–2, pp. 177–182, 2009.

[30] T. S. Bjørheim, S. Stølen, and T. Norby, “Ab initio studies of hydrogen and acceptor defects in rutile TiO_2,” *Phys. Chem. Chem. Phys.*, vol. 12, no. 25, p. 6817, 2010.

[31] H. Kamisaka and K. Yamashita, “Theoretical Study of the Interstitial Oxygen Atom in Anatase and Rutile TiO_2: Electron Trapping and Elongation of the r (O− O) Bond,” *J. Phys. Chem. C*, vol. 115, pp. 8265–8273, 2011.

[32] H.-X. Deng, S.-S. Li, J. Li, and S.-H. Wei, “Effect of hydrogen passivation on the electronic structure of ionic semiconductor nanostructures,” *Phys. Rev. B*, vol. 85, no. 19, pp. 1–5, 2012.

[33] X. Liu, G. Zhu, X. Wang, X. Yuan, T. Lin, and F. Huang, “Progress in Black Titania: A New Material for Advanced Photocatalysis,” *Adv. Energy Mater.*, vol. 6, no. 17, pp. 1600452, 2016.

[34] S. S. Ataei, M. R. Mohammadizadeh, and N. Seriani, “Ab Initio Simulation of the Effects of Hydrogen Concentration on Anatase TiO_2,” *J. Phys. Chem. C*, vol. 120, no. 16, pp. 8421–8427, 2016.

[35] A. Rockett, *The materials science of semiconductors*. McGraw-Hill , 2008.

[36] R. H. Bube and H. E. MacDonald, “Effect of photoexcitation on the mobility in photoconducting insulators,” *Phys. Rev.*, vol. 121, no. 2, pp. 473–483, 1961.

[37] D. C. Hurum, a G. Agrios, K. a Gray, T. Rajh, and M. C. Thurnauer, “Explaining the enhanced photocatalytic activity of Degussa P25 mixed-phase TiO_2 using EPR,” *J. Phys. Chem. B*, vol. 107, no. 19, pp. 4545–4549, 2003.

[38] X. Jiang *et al.*, “Characterization of Oxygen Vacancies Associates within the Hydrogenated TiO_2 : a Positron Annihilation Study Characterization of Oxygen Vacancies Associates within the Hydrogenated TiO_2 : a Positron Annihilation Study,” *J. Phys.Chem.C*, vol. 116, pp. 22619–22624, 2012.

[39] H. Yin *et al.*, “Gray TiO_2 nanowires synthesized by aluminum-mediated reduction and their excellent photocatalytic activity for water cleaning,” *Chem. - A Eur. J.*, vol. 19, no. 40, pp. 13313–13316, 2013.

[40] L. R. Grabstanowicz *et al.*, “Facile Oxidative Conversion of TiH_2 to High-Concentration Ti^{3+}-Self- Doped Rutile TiO_2 with Visible-Light Photoactivity,” *Inorg. Chem.*, vol. 52, p. 3884−3890, 2013.

[41] F. M. Pesci, G. Wang, D. R. Klug, Y. Li, and A. J. Cowan, “Efficient Suppression of Electron − Hole Recombination in Oxygen- Deficient Hydrogen-Treated TiO_2 Nanowires

for Photoelectrochemical Water Splitting," *J. Phys. Chem. C*, vol. 117, p. 25837, 2013.

[42] J. Dong *et al.*, "Defective black TiO_2 synthesized via anodization for visible-light photocatalysis," *ACS Appl. Mater. Interfaces*, vol. 6, no. 3, pp. 1385–1388, 2014.

[43] X. Liu *et al.*, "Ti3+ self-doped TiO_{2-x} anatase nanoparticles via oxidation of TiH2 in H2O2," *Catal. Today*, vol. 225, pp. 80–89, 2014.

[44] W. Wei, N. Yaru, L. Chunhua, and X. Zhongzi, "Hydrogenation of TiO_2 nanosheets with exposed {001} facets for enhanced photocatalytc activity," *RSC Adv.*, vol. 2, no. 22, pp. 8286–8288, 2012.

[45] L. R. Grabstanowicz *et al.*, "Facile oxidative conversion of TiH_2 to high-concentration Ti^{3+}-self-doped rutile TiO_2 with visible-light photoactivity," *Inorg. Chem.*, vol. 52, no. 7, pp. 3884–3890, 2013.

[46] C. Zhang *et al.*, "Supported noble metals on hydrogen-treated TiO_2 nanotube arrays as highly ordered electrodes for fuel cells," *ChemSusChem*, vol. 6, no. 4, pp. 659–666, 2013.

[47] H. Guo, W. Wang, L. Liu, Y. He, C. Li, and Y. Wang, "Shape-controlled synthesis of Ag TiO_2 cage-bell hybrid structure with enhanced photocatalytic activity and superior lithium storage," *Green Chem.*, vol. 15, no. 10, p. 2810, 2013.

[48] Z. Zheng *et al.*, "Hydrogenated titania: synergy of surface modification and morphology improvement for enhanced photocatalytic activity," *Chem. Commun.*, vol. 48, no. 46, p. 5733, 2012.

[49] M. Z. Jacobson *et al.*, "Hydrogenated TiO_2 Nanotube Arrays for Supercapacitors," *Energy Environ. Sci.*, vol. 8, no. 7, pp. 2093–2117, 2015.

[50] C. Yang *et al.*, "Core-shell nanostructured 'black' Rutile Titania as excellent catalyst for hydrogen production enhanced by sulfur doping," *J. Am. Chem. Soc.*, vol. 135, no. 47, pp. 17831–17838, 2013.

[51] C. Fan *et al.*, "Black Hydroxylated Titanium Dioxide Prepared via Ultrasonication with Enhanced Photocatalytic Activity," *Sci Rep*, vol. 5, no. July, p. 11712, 2015.

[52] M. Tian *et al.*, "Structure and Formation Mechanism of Black TiO_2 Nanoparticles," *ACS Nano*, no. 10, pp. 10482–10488, 2015.

[53] H. Cui *et al.*, "Black TiO_2 nanotube arrays for high-efficiency photoelectrochemical water-splitting," *J. Mater. Chem. A*, vol. 2, no. 23, pp. 8612–8616, 2014.

[54] P. Raghunath, W. F. Huang, and M. C. Lin, "Quantum chemical elucidation of the mechanism for hydrogenation of TiO_2 anatase crystals," *J. Chem. Phys.*, vol. 138, no. 15, 2013.

[55] J. Lu, Y. Dai, H. Jin, and B. Huang, "Effective increasing of optical absorption and energy conversion efficiency of anatase TiO_2 nanocrystals by hydrogenation.," *Phys. Chem. Chem. Phys.*, vol. 13, no. 40, pp. 18063–8, 2011.

[56] J. Chen and W. Wang, "Carrier transport processes in dye sensitized solar cells based on Zn_2SnO_4 nanostructures studied by intensity modulated photocurrent/photovoltage spectroscopy," *Appl. Phys. Lett.*, vol. 102, no. 21, p. 213904, 2013.

[57] F. Zuo, L. Wang, T. Wu, Z. Zhang, D. Borchardt, and P. Feng, "Supporting information Self-doped Ti^{3+} Enhanced Photocatalyst For Hydrogen Production Under Visible-light," *J. Am. Chem. Soc.*, vol. 132, pp. 11856–11857, 2010.

[58] D. Kumar Behara *et al.*, “Coupled optical absorption, charge carrier separation, and surface electrochemistry in surface disordered/hydrogenated TiO_2 for enhanced PEC water splitting reaction,” *Phys. Chem. Chem. Phys. Phys. Chem. Chem. Phys. Accept. Manuscr.*, vol. 18, pp. 8364–8377, 2016.

[59] P. Yan *et al.*, “Photoelectrochemical water splitting promoted with a disordered surface layer created by electrochemical reduction,” *ACS Appl. Mater. Interfaces*, vol. 7, no. 6, pp. 3791–3796, 2015.

Chapter 4: Experimental Methods and Materials

4.1 Electrode Synthesis:

Nanotubes are known of their directional charge transfer which allow for better charge collection [1], while nanospheres are known of their high surface area to volume ratio which speed up the catalytic reactions. We may combine both advantages of directional charge transfer and high surface area in an oval shaped sub 100 nm nanotubular structure [2]. Briefly, pure titanium foil samples were ultrasonically cleaned in acetone, ethanol, and then water. Anodization of the foils was carried out in two-electrode cells, with the titanium foils as the working electrode and platinum foil as the counter electrode as shown in Figure 4.1. The electrolyte was prepared by mixing 1% NH_4F **(**Sigma-Aldrich, $ 98%) with 1.1 wt% polyvinylpyrrolidone (MW ~40 000, Loba Chemie) and 0.75 wt% H_2O in a formamide-based electrolyte using a galvanostatic anodization method for 2.5 h at 0 ℃. The pH of the electrolyte was controlled by the addition of 0.1 M acetic acid to the solution. Prior to anodization, the electrolyte was stirred for 1.15 h at 100 ℃. The As-anodized samples were annealed in air, Hydrogen, and Oxygen using a Thermo-Scientific LINDBURG/BLUE M TF55030C tube furnace at 450 °C for 2 h, with up/down rates of 1 °C/min.

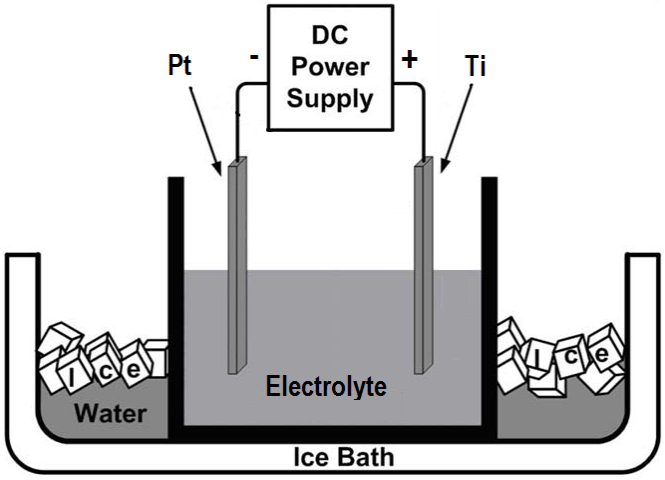

Figure 4.1: Anodization setup.

4.2 Electrodes Characterization

The fabricated nanotubes have a diameter of 20 ± 3 nm as shown in Figure 4.2a and d with an average length of 70 ± 10 nm. To further ensure the tubular nature of the structure, the nanotubes were peeled of the Ti foil and examined under TEM as shown in Figures 4.2 b and e. Figure 4.2c shows the HR-TEM which reveals the partial crystallinity of TiO_2 while the inset in Figure 4.2f presents the lattice distance of the structure which is 0.4 nm corresponding to anatase.

X-ray photoelectron spectroscopy (XPS) was performed in an ultrahigh vacuum chamber (UHV) equipped with a monochromatic Al Kα (1486.6eV), X-Ray source and a SPHERA U7 hemispherical analyzer. The total energy resolution of the X-ray source was equal to 0.1 eV. While for acquiring the survey spectrum and the high resolution core level peaks for the various elements, the X-ray Source was tuned to be 40 and 20 eV, respectively. A Shimadzu UV-3600 UV-Vis- NIR spectrophotometer with integrated sphere was used for optical characterization. The phase and local structural details of TiO_2 were obtained from the Raman spectroscopy with a 532 nm excitation wavelength laser beam.

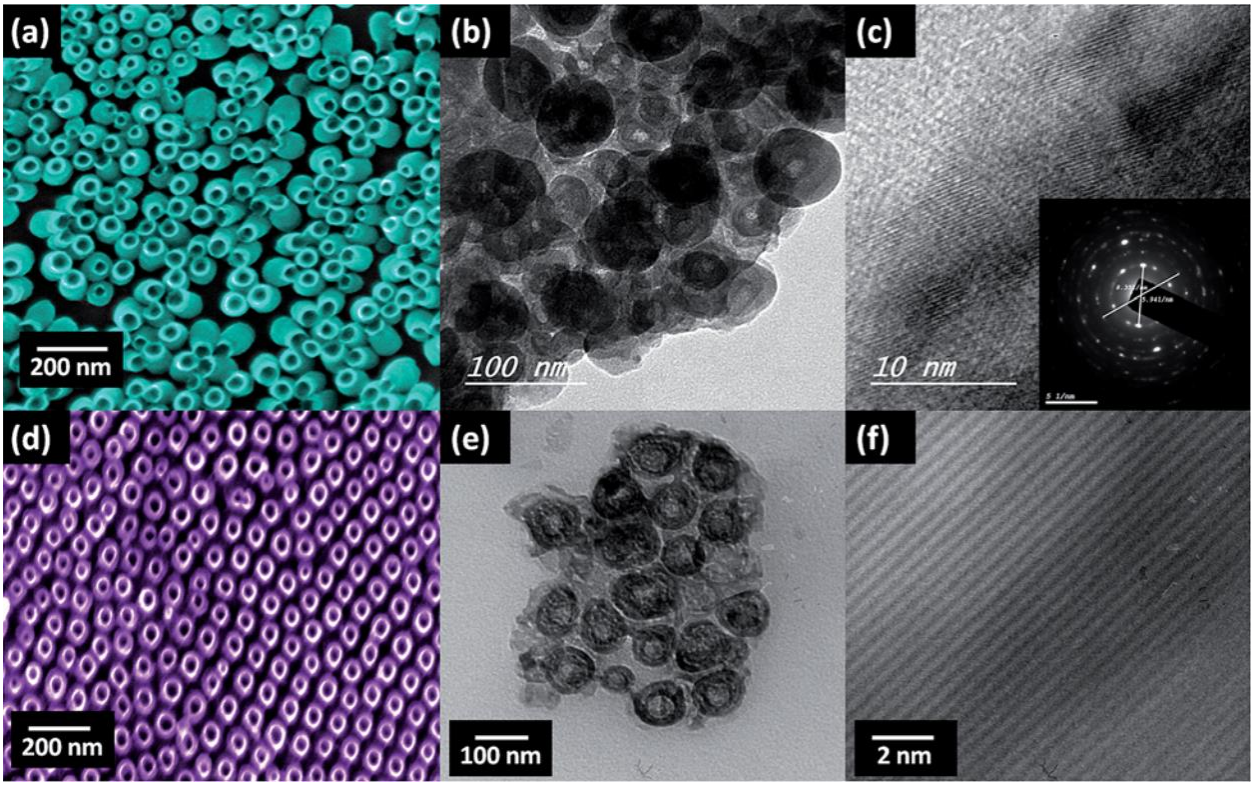

Figure 4.2: a) SEM, b) TEM, and c) HR-TEM images of the as-anodized samples while (d) SEM, (e) TEM, and (f) HR- TEM images of the samples annealed at 400 °C. [2]

4.3 Photoelectrochemical Analysis

Photoelectrochemical properties of the samples were investigated using a three-electrode configuration, with the TiO_2 nanotube array photo anode as a working electrode, saturated Calomel as a reference electrode, and platinum foil as a cathode as shown in Figure 4.3. To measure dark and illuminated currents at a scan rate of 0.05 Vs^{-1}, a scanning potentiostat (Biologic SP-200) was used with an applied bias from 0 V to 1.2 V vs SCE supplied to the anode. Sunlight was simulated using a 300 W ozone-free xenon lamp and AM 1.5G filter at 100 mW cm^{-2}. Impedance spectra were measured at different applied potentials versus SCE and fitted to equivalent circuits using Z-

fit software. The IPCE experiments were conducted in a two- electrode cell under no applied bias with the nanotube film as the working photoelectrode and platinum foil as the counter electrode in 1.0 M KOH solution.

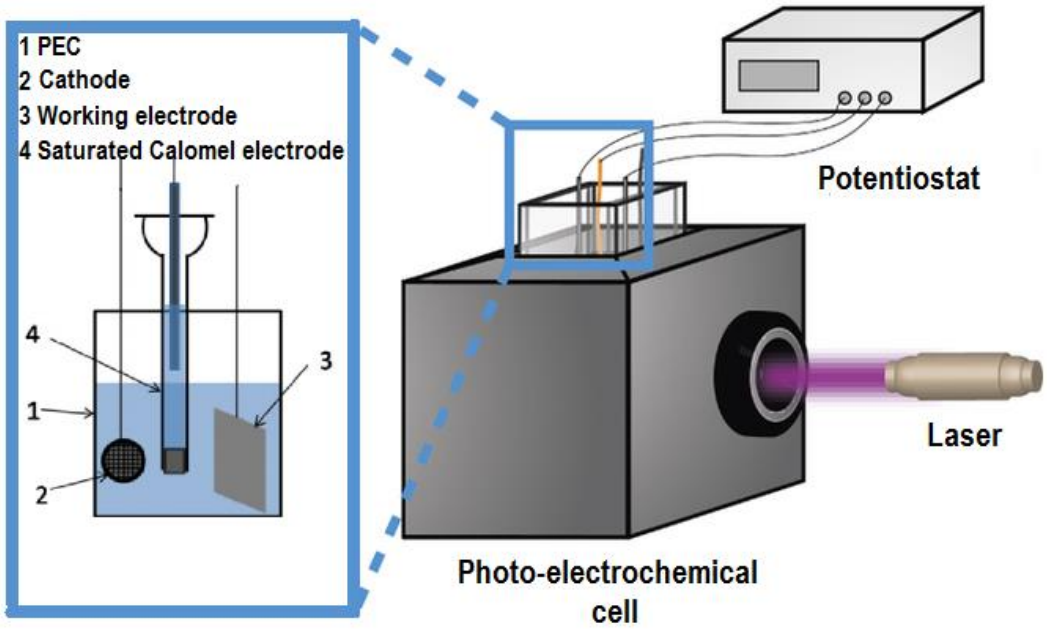

Figure.4.3: Photo-electrochemical cell connected to potientiostat.

References

[1] Y. Liu, B. Zhou, J. Li, X. Gan, J. Bai, and W. Cai, "Preparation of short, robust and highly ordered TiO_2 nanotube arrays and their applications as electrode," *Appl. Catal. B Environ.*, vol. 92, no. 3–4, pp. 326–332, 2009.

[2] M. Samir, M. Salama, and N. K. Allam, "Sub-100 nm TiO_2 tubular architectures for efficient solar energy conversion," *J. Mater. Chem. A*, vol. 4, no. 24, pp. 9375–9380, 2016.

Chapter 5: Results and discussion

5.1 Chemical Analysis

It is well-known that, aside from cases of very low oxygen partial pressures where interstitial Ti^{n+} ions dominate, oxygen vacancies are the major type of donating defects in TiO_2 [1]. Thus, oxygen-deficiency within the lattice of TiO_2 has been extensively used as evidence for the increase in donor density [2], [3]. To understand the extent of oxygen-deficiency within our samples, XPS core spectra were collected. Figures 5.1- 5.5 show Ti 2p and O 1s core spectra, respectively. As shown, red and blue shifts in the Ti 2p and O 1s spectra, respectively, can be observed in all hydrogen-annealed samples. This can be related to the increase in oxygen-vacancies, where Ti^{4+} ions gain back some of their electrons forming Ti^{n+} ($n<4$), which should have lower binding energies. On the other hand, oxygen ions exhibit more competitiveness over its electrons due to their increased deficiency, which would result in higher electron binding energies. Focusing on Ti 2p spectra, all samples show doublet peaks (464.2-6 eV for $2p_{1/2}$ and 458.5-9 eV for $2p_{3/2}$) within range of standard data, [4] although the red shifts in the hydrogen-annealed samples lead to binding energies (<458.6 eV) that were attributed before to Ti^{3+} states close to oxygen vacancies [5]. Turning to O 1s spectra, air- and oxygen-annealed samples exhibited peaks centered at 529.7 eV, characteristic of lattice oxygen [4], [6] with stoichiometries of $TiO_{1.9}$ and TiO_2 respectively. As expected, oxygen annealing has neutralized most of the oxygen vacancies in the crystal lattice increasing the concentration of Ti^{4+} and reducing the donor density. One can observe a strong peak in the oxygen-annealed sample centered at 532.5 eV which is assigned to the full oxidation of adventitious carbon species [7] deposited on the sample's surface during anodization in an organic electrolyte, handling of the samples and cleaning using ethanol [8]. Considering hydrogen

annealed samples, the reducing atmosphere created by hydrogen gas induced structural defects in the form of increased concentration of oxygen vacancies [9]–[13] which is inferred when observing the stoichiometry resulting from different hydrogen flow rates. For H_2 50 and H_2 100, the calculated stoichiometries were nearly the same $TiO_{1.7}$ while for H_2 150 the stoichiometry was $TiO_{1.4}$.

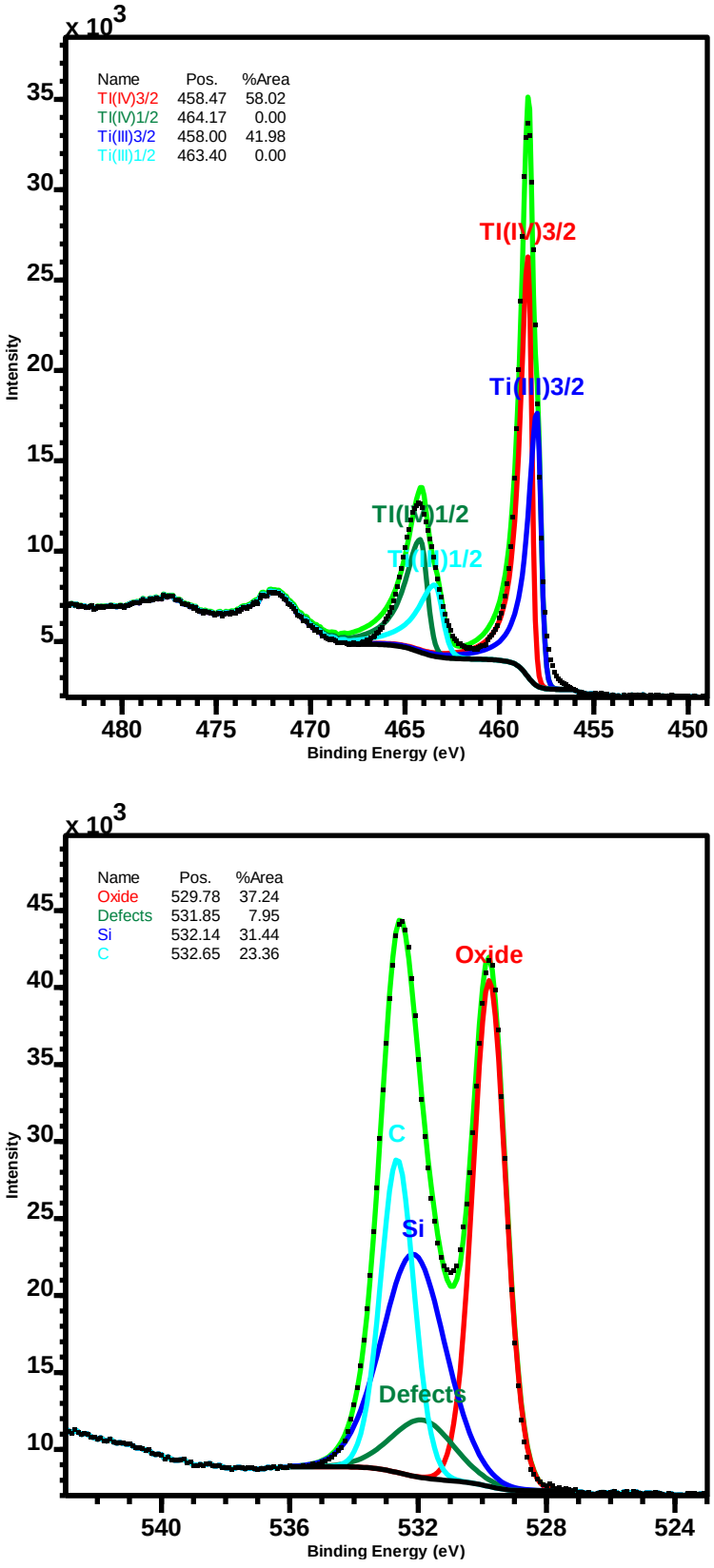

Figure 5.1: XPS core spectra of Ti 2p (upper) and O 1s (lower) for oxygen annealed samples

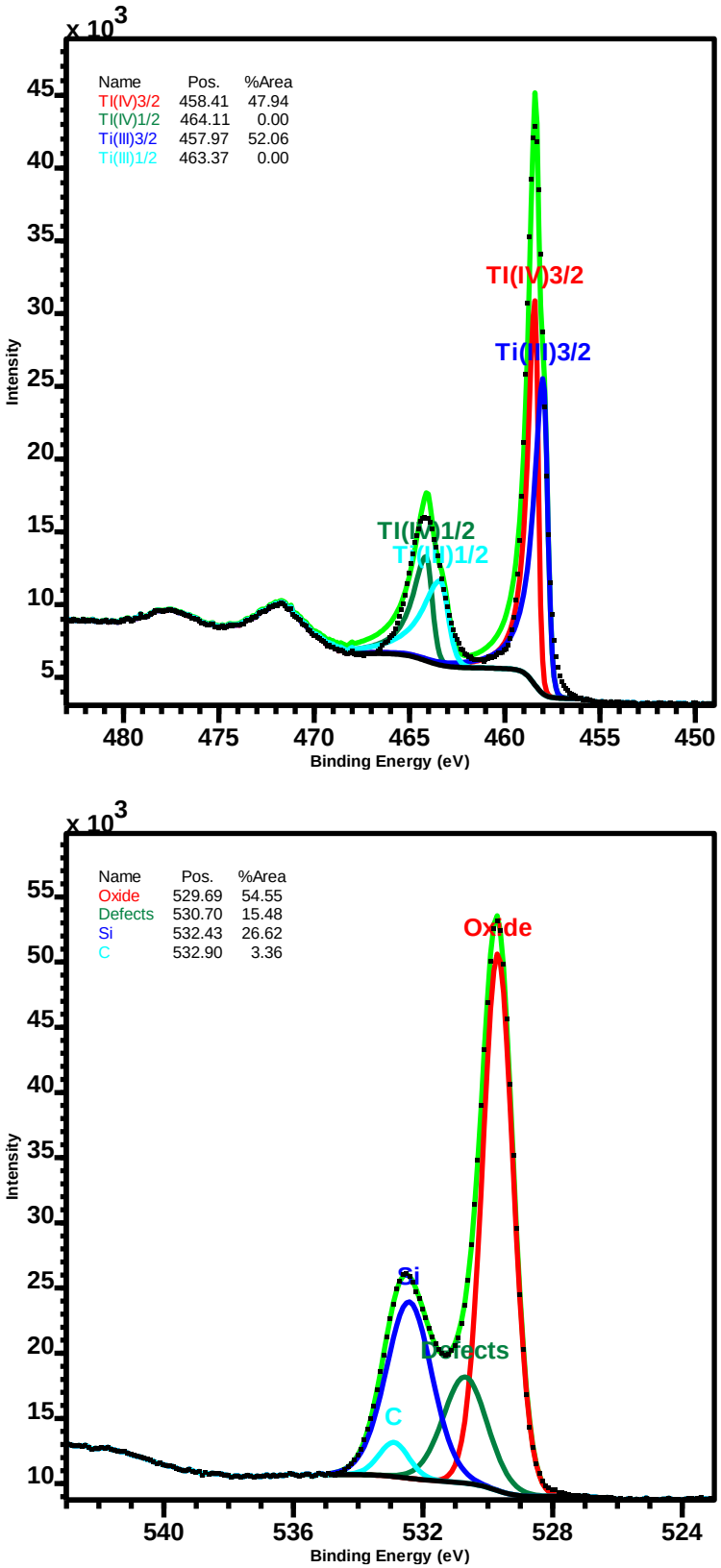

Figure 5.2: XPS core spectra of Ti 2p (upper) and O 1s (lower) for air annealed samples

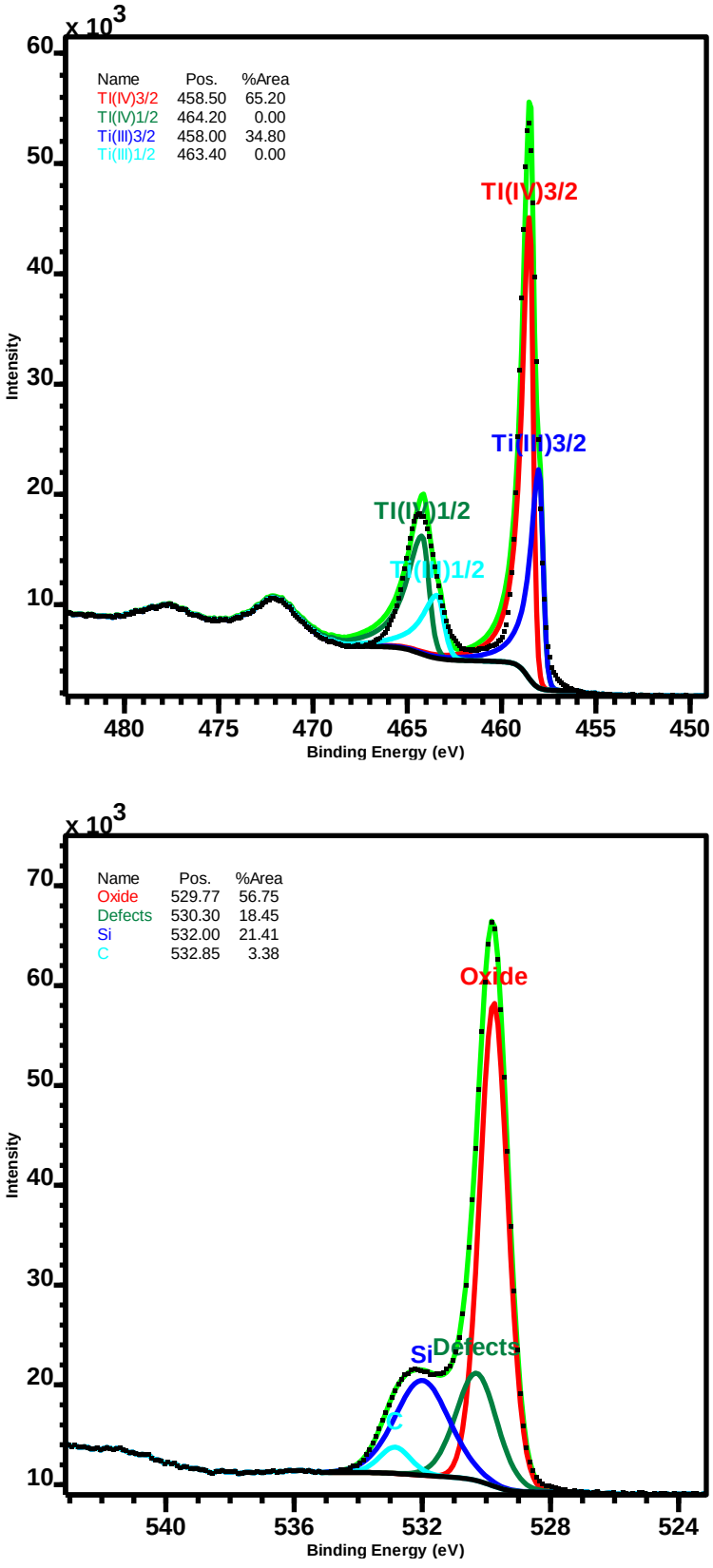

Figure 5.3: XPS core spectra of Ti 2p (upper) and O 1s (lower) for H50

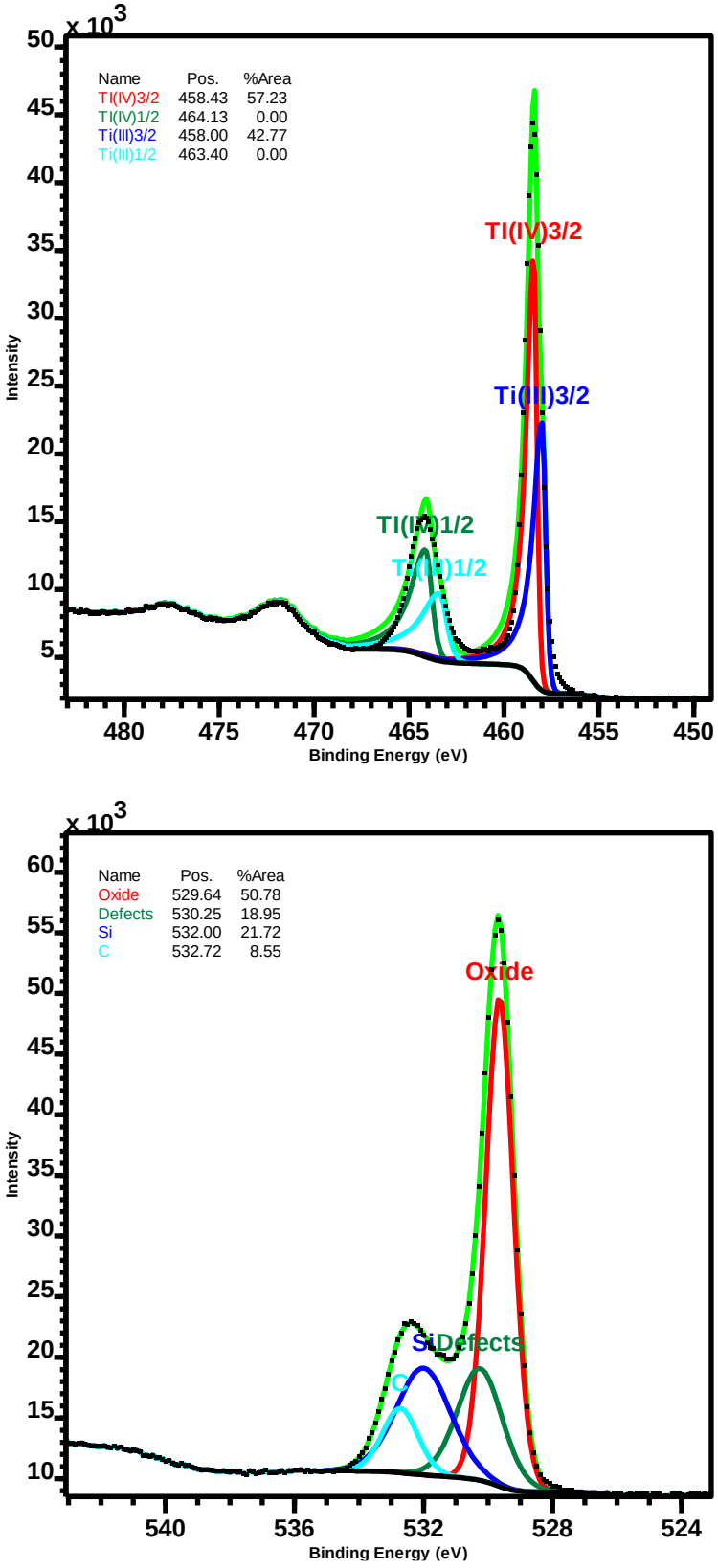

Figure 5.4: XPS core spectra of Ti 2p (upper) and O 1s (lower) for H100

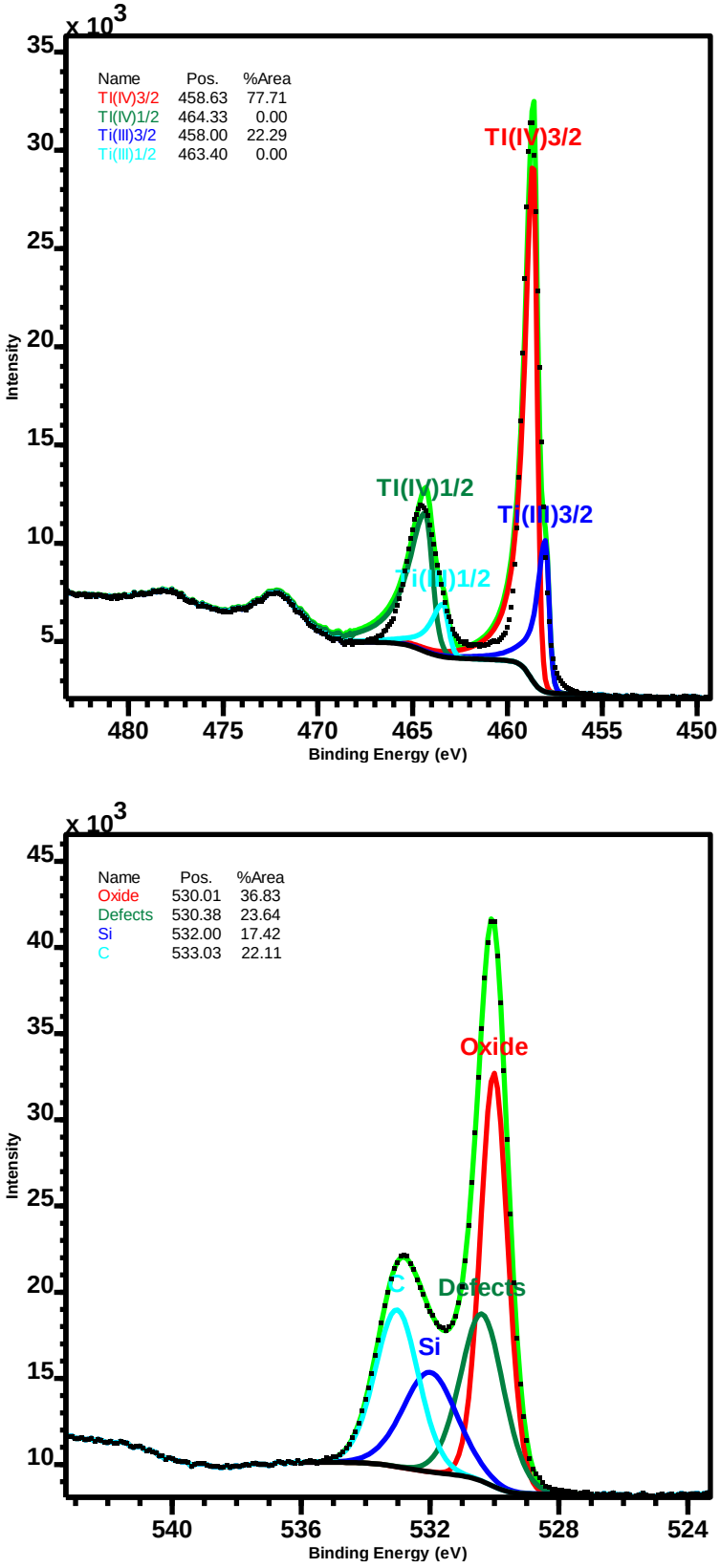

Figure 5.5: XPS core spectra of Ti 2p (upper) and O 1s (lower) for H150

5.2 Optical Characterization

The position of defect states inside black TiO_2 can greatly affect its band gap, making optical characterization a primary tool in mapping defect chemistry of semiconductors. As such, UV-Vis and Raman spectra were collected for all samples. As shown in Figure 5.6, air and oxygen-annealed samples exhibited sharp drops in absorption close to the fundamental band gap of TiO_2. Notable is the slow rise in absorbance of the Air-annealed samples alone towards lower photon energies, which was previously attributed to inter-band gap defects [14]. Without a shift in the absorption edge, H50 samples exhibited a sharper rise towards higher wavelengths, indicative of abundance of defect states. Interestingly, H100 and H150 samples showed a similar, yet much-later rise in absorbance (not displayed here) starting at 550-600 nm. This was preceded by a broader absorption edge that fully decayed in the 500-550 nm range, clearly indicating visible-light absorption of these samples. Comparison of the latter decay with the observed rise of absorbance in the H50 samples, within the exact same range of energies, implies different natures of defect states in these samples, where deep trap states attract electrons, thus possibly showing low energy absorption peaks. This phenomenon seems to be absent in the H100 and H150 samples.

Table 5.1 lists the Tauc analysis data, presenting the band gaps of different samples. The reduction in band gap has been attributed before to the creation of conduction and valence band tails due to surface distortion as a result of annealing in heavily-reducing atmospheres [15] like those exhibited in high flow rates of H_2 gas during annealing. The question of the nature of this defect band being different than, for instance, discrete defect states present in the H50 samples is still un-answered.

Table 5.1: Calculated band gap for every annealing atmosphere of different samples.

Annealing atmosphere	*Bandgap (ev)*
Air	*3.34*
O_2	*3.37*
H50	*3.31*
H100	*2.41*
H150	*2.45*

Figure 5.7 shows the Raman spectra of the annealed samples. Note the difference in intensities between Air and H50 samples compared to the O_2, H100, and H150 set of samples. The reason maybe the difference in phases between both sets of samples, with the Air and H50 samples showing pure anatase structure, while rutile phase appears in the other three conditions, diminishing the intensity of anatase peaks. More importantly are the phonon lifetimes, shown in the left inset of Figure 5.7, where long phonon lifetimes in H50 samples are a direct indication of increased scattering of electrons [16]. The origin of this observation can be the presence of structural defects inside the lattice that hinder charge diffusion. In contrast, H100 and H150 samples showed the shortest phonon lifetimes, with the latter having slightly longer-living phonons than the former. Although this seems to be in line with the conclusion drawn above about a change in the nature of defects in black TiO_2 nanostructures, the conclusion that more reducing atmospheres lead to less lattice distortion seems contradicting with the literature.

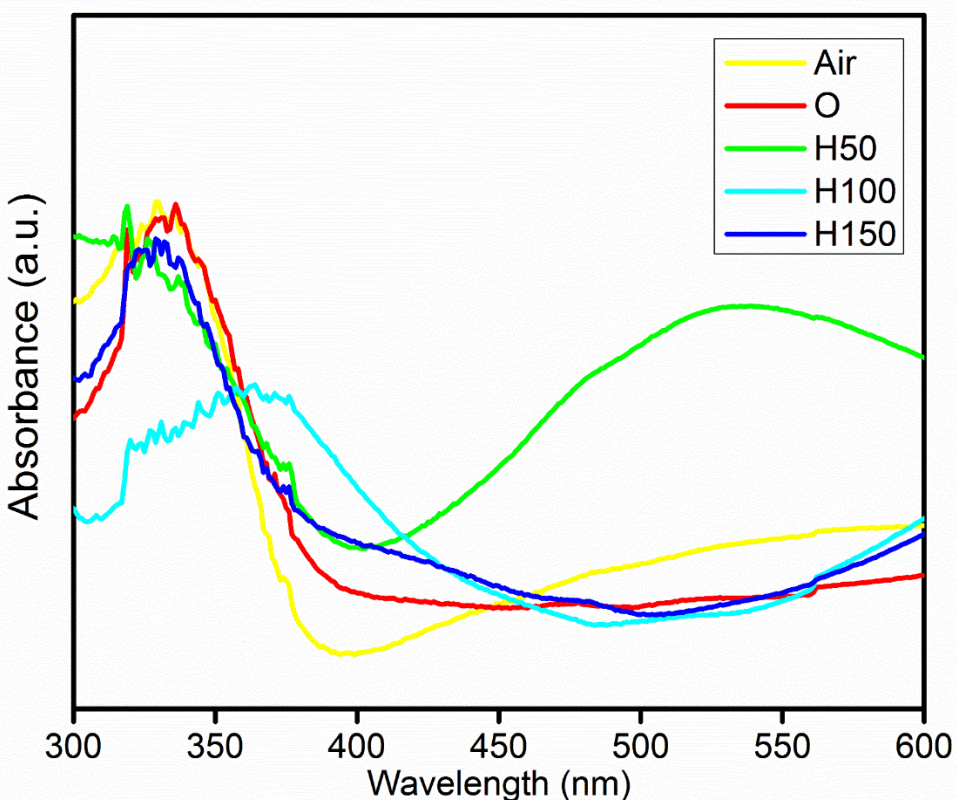

Figure 5.6: UV-Vis absorbance spectra of different annealing conditions

However, a thorough analysis of the Raman spectra can resolve this discrepancy. The calculated rutile/anatase phase ratios for all 5 sub-100 nm TiO_2 array samples are listed in Table 5.2. Oxygen-annealed samples were mostly rutile, given the relatively high annealing temperature for such short nanotubes, [17] coupled with the highly-oxidizing atmosphere, which should assist in rutile crystallite growth as previously reported [18]. Regarding the hydrogen-annealed samples, Bak et al. [19] have predicted that, although both types of defects generally arise, Ti^{3+} interstitials are the dominant donor defect type in TiO_2 under heavily-reducing atmospheres, not oxygen vacancies. These interstitial ions were said to hinder atomic transport in anatase TiO_2, [20] leading to a delayed anatase-to-rutile transformation. On the other hand, it has also been reported that

anatase-to-rutile phase transformation starts at oxygen vacancies, where the energy needed to reorder the atoms is relatively small [21], [18]. With the abundance of oxygen vacancies being one of the main outcomes of hydrogen-annealing of TiO_2, [9]–[13] anatase-to-rutile transformation dynamics is perturbed. The larger structural disturbance in the H50 samples, as evident from the longest phonon lifetimes, should have suppressed the anatase-to-rutile transformation, even at these high temperatures. Increasing the extent of reduction, although expected to increase Ti^{3+} interstitials according to the model proposed by Bak et al. [19] leads to an increase of the density of oxygen vacancies to an extent that allow rutile nucleation and growth. The latter process should result in re-ordering of the lattice, and thus allowing for better charge transport, as evident from the shortest phonon lifetime. Note that this transformation was not accompanied by loss of visible-light absorption as that with oxygen-annealed samples. Optical characterization shows the abundance of structural defects in anatase H50 samples that may act as trap states, while H100 and H150 samples show extended visible-light absorption and less structural distortion. From tables 4.1 and 4.2 H150 has slightly larger band gap as well as rutile/anatase ratio compared to H100 which further confirms that anatase to rutile transformation reduces structural defects and thereby, decreases conduction and valence band tailing resulting in a wider band gap. The deduced relation between the increase in rutile phase content with increasing reduction of annealing atmosphere, and the decrease in trap state density is yet to be confirmed.

Table 5.2: Rutile-to- anatase ratio of different samples

Annealing atmosphere	*Rutile/Anatase*
Air	0.0
O_2	16.0
H50	0.0
H100	3.1
H150	4.8

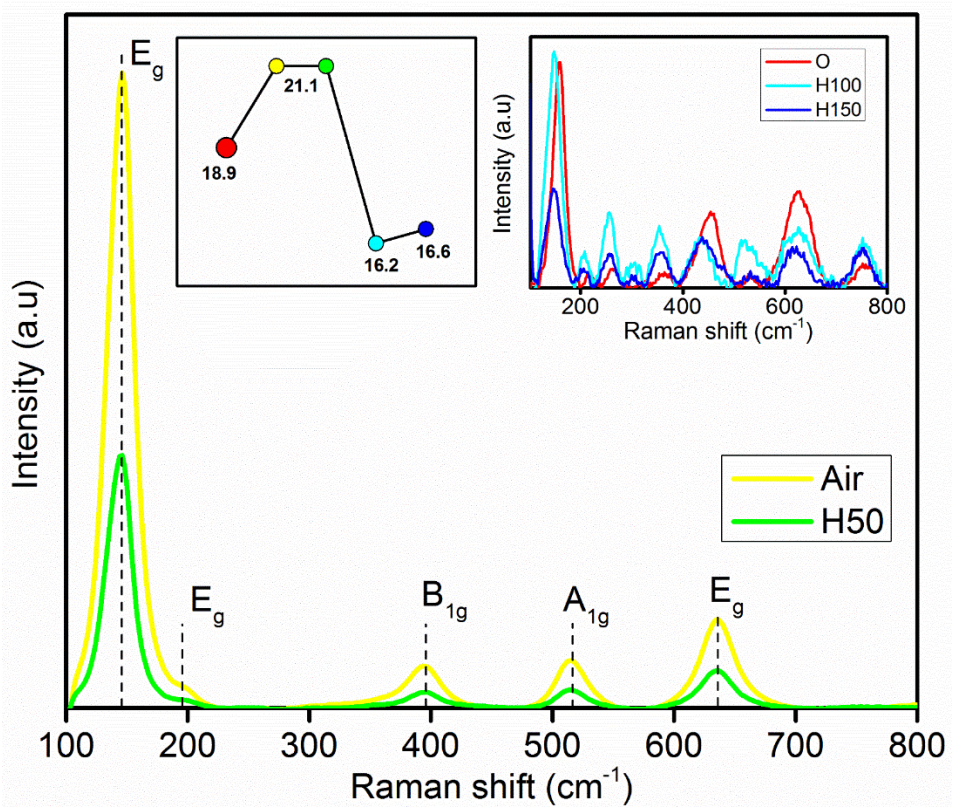

Figure 5.7: Raman spectra of Air (yellow) and H50 (green) samples. The inset in shows the Raman spectra of the O (red), H100 (cayan) and H150 (Blue) samples.

5.3 Photoelectrochemical Analysis

As the ultimate effect of trap states in a material is the deterioration of its photocatalytic performance, the photocurrent characteristics of the materials were investigated. Figure 5.8a shows *J-V* plots for sub-100 nm 1D TiO_2 structures annealed under different atmospheres. The air-annealed samples exhibited the least photocurrent, followed by oxygen-annealed counterpart. Annealing under different flow rates of H_2 leads to an initial increase in photocurrent reaching ~2 orders of magnitude for samples annealed under 100 sccm H_2 compared to the air-annealed counterparts. Note that the dark currents show almost the same trend, see the top inset in Figure 5.8a. Increasing the flow rate till 150 sccm leads to a substantial loss of both dark and photocurrents. A thorough analysis of the photocurrent behavior of H_2-annealed samples indicates a delay in the onset potential, implying the need for more potential to separate all charge carriers within the space charge layer [22]. This may be a direct indication of increased donor states with increasing H_2 flow rate. Furthermore, Allam et al. [23] showed that an increase in dark currents surpassing that in photocurrents may indicate, aside from diminished photoactivity, the abundance of trap states compared to their shallow donor counterparts. They had also suggested a defect sensitivity factor (S) describing this phenomenon that can be expressed as: [23]

$$S = \frac{C_{dark}}{C_{light}} \qquad 5.1$$

where *C* is the current density shift term, comparing the dark/photocurrent of samples annealed under certain gas, to those annealed under air [23]. Calculating this factor for our samples (bottom inset in Figure 5.8a, the H100 samples showed the least amount of trap states, followed by H50 samples. The H150 samples showed the greatest increase in dark currents *versus* that in photocurrents compared to air-annealed samples. Note that oxygen-annealed samples showed Figures less than 1 owing to the decrease in defect density (e.g. oxygen vacancies) in the highly-

oxidizing atmosphere. This trend explains, to some extent, the observed photocurrent behavior, where the decreased abundance of localized trap states in H100 samples allowed for the highest charge collection as compared to the H50 and H150 counterparts. Also, the photocurrents of all hydrogen-annealed samples, being higher than that for oxygen samples, dictate that such trap states are accompanied by the creation of beneficial donor states under hydrogen-rich atmosphere. These observation are in agreement with the conclusions drawn from the optical characterization for H100 samples. There remains now to explain the diminished behavior of samples annealed under 150 sccm H_2 flow compared to their H50 counterparts.

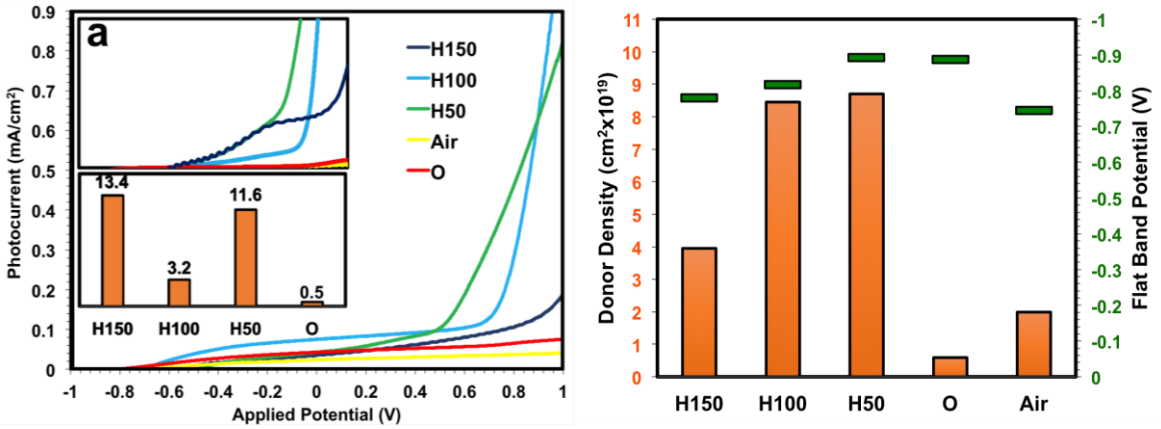

Figure 5.8: (a) J-V plots for sub-100 nm 1D TiO_2 structures annealed under different atmospheres with the lower inset presents defect sensitivity factor of different samples, and (b) Donor density of different samples on the left axis and the flat band potential shown on the right axis.

To this end, Mott-Schottky plots were extracted from the electrochemical impedance spectroscopy measurements in order to understand the defect distribution in the samples. Figure 5.8b shows the variation of flat band potential (V_{FB}) and the donor density (N_D) of the samples annealed in different atmospheres. Note that air-annealed samples showed the most anodic V_{FB}, which was expected given the widely-known position of oxygen vacancy defect states (0.7-1.2 eV

below the CBM) [3], [24]–[28]. It is expected that the Fermi level would be situated around such donor states. Oxygen annealing, on the other hand, shifted the Fermi level towards the CBM owing to the annihilation of oxygen vacancies. This aside, the behavior of hydrogen-annealed samples showed the same trend in N_D and V_{FB}, where H50 samples showed the highest density of donor states, as well as the most cathodic Fermi level, followed by H100 samples, then H150. These results closely fit the arguments presented above. Firstly, with the abundance of defect states in the H50 sample, many of which must be donating electrons to the CBM as evident from the high photocurrent, which would shift the Fermi level upward (more cathodic potentials *versus* NHE). Secondly, with the heavily-reducing atmospheres of the H100 and H150 samples, as discussed before, rutile phase nucleation and growth occurred, lowering the CBM of anatase and re-arranging the atoms inside the lattice to give less defect density and better charge transport. However, the extended anatase-to-rutile transformation in H150 samples leads to a deterioration in the photocatalytic performance, owing to the less-activity of rutile phase towards solar water splitting [29]. This explains the lowest V_{FB}, as well as the relatively low photocurrent, and relatively high dark current. Another reason for the diminishing performance of H150 samples can be explained in terms of the position from which rutile phases nucleate. Allam et al. [20] have previously proved that rutile phases originate from the metal substrate moving upwards towards the oxide nanotube arrays. Similar to our observations, initial increase in rutile/anatase ratios of their samples enhanced photocatalytic performance, followed by photocurrent deterioration at high rutile contents. They explained that phenomenon *via* the densification of the rutile crystallites beneath the TiO_2 nanotubes, which may have blocked charge carriers trying to reach the metal electrode [18]. However, note that our samples did not show any structural damage as can be seen from the SEM images of the sub-100 nm structures before and after annealing in the different atmospheres

(Figure 5.9). Consequently, it is safe to conclude that anatase-to-rutile transformation can play an important role in decreasing the density of trap states, without greatly annihilating beneficial shallow donor states. However, high rutile contents can deteriorate the effect of those donor states for one or more of the following: 1) either through extended annihilation of these shallow states, or 2) through creating charge carrier traps at the interface of substrate and the oxide, or 3) simply due to the less-activity of the rutile phase towards water splitting.

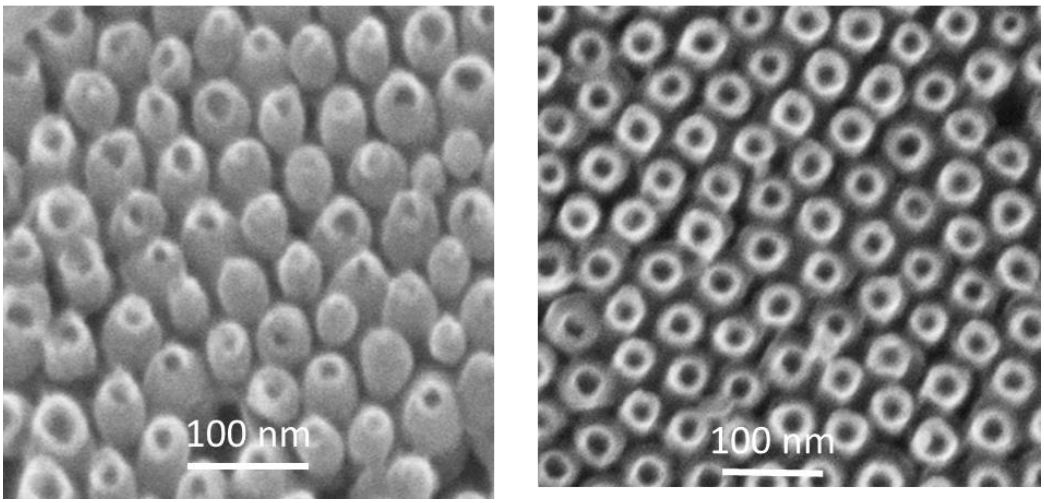

Figure 5.9: SEM image of as-anodized (left) and H100 (right) sub-100 nm TiO_2 nanotubes

Finally, with the optimized electrode dimensions of the sub-100 nm TiO_2 structures, and the optimized electronic characteristics of the H100 modification scheme, 2-electrode incident photon to current efficiency (IPCE) analysis was performed to investigate the charge collection characteristics, Figure 5.10. The H100 samples showed the highest IPCE values (~30%) followed by H150 samples (~ 23%) and finally the H50 samples. The hydrogen annealed samples super pass the air-annealed counterparts as a result of excess oxygen vacancies induced by annealing in a reducing atmosphere. Those vacancies are responsible for the increased number of free carriers that promote water splitting reaction. However, when TiO_2 is subject to heavily reducing

atmosphere (as in H150), the atomic crystal starts to rearrange in rutile phase that is less-active toward water splitting. While the high rutile content in the H150 sample might be responsible for hindering the charge transport as indicated via the IPCE performance, the high concentration of defects degrades the performance of the H50 samples. Therefore, the H100 sample seems to strike a balance between lower rutile content, compared to H150, and lower concentration of defects, relative to H50, which might explain why H100 achieves the highest IPCE.

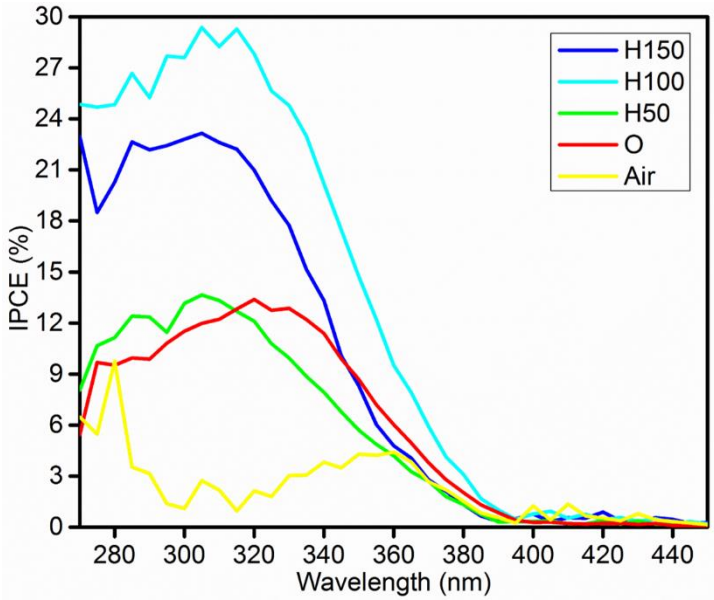

Figure 5.10: Incident Photon to current conversion efficiency of the samples annealed under different annealing conditions

References

[1] T. Bak, J. Nowotny, M. Rekas, and C. C. Sorrell, "Defect chemistry and semiconducting properties of titanium dioxide: I. Intrinsic electronic equilibrium," *J. Phys. Chem. Solids*, vol. 64, no. 7, pp. 1043–1056, 2003.

[2] H. Cui *et al.*, "Black TiO_2 nanotube arrays for high-efficiency photoelectrochemical water-splitting," *J. Mater. Chem. A*, vol. 2, no. 23, pp. 8612–8616, 2014.

[3] G. Wang *et al.*, "Hydrogen-treated TiO_2 nanowire arrays for photoelectrochemical water splitting," *Nano Lett.*, vol. 11, no. 7, pp. 3026–3033, 2011.

[4] J. R. Rumble, D. M. Bickham, and C. J. Powell, "The NIST x-ray photoelectron spectroscopy database," *Surf. Interface Anal.*, vol. 19, no. 1–12, pp. 241–246, Jun. 1992.

[5] R. P. Antony, T. Mathews, S. Dash, A. K. Tyagi, and B. Raj, "X-ray photoelectron spectroscopic studies of anodically synthesized self aligned TiO_2 nanotube arrays and the effect of electrochemical parameters on tube morphology," *Mater. Chem. Phys.*, vol. 132, no. 2–3, pp. 957–966, 2012.

[6] L. Chen, F. He, Y. Huang, Y. Meng, and R. Guo, "Hydrogenated nanoporous TiO_2 film on Ti-25Nb-3Mo-2Sn-3Zr alloy with enhanced photocatalytic and sterilization activities driven by visible light," *J. Alloys Compd.*, vol. 678, pp. 5–11, 2016.

[7] D. Beamson, G.; Briggs, *High-Resolution Spectra of Organic Polymers: The Scienta ESCA300 Database*. Chichester [England] ; Wiley, 1992.

[8] G. Ketteler *et al.*, "The Nature of Water Nucleation Sites on TiO 2 (110) Surfaces Revealed by Ambient Pressure X-ray Photoelectron Spectroscopy," *J. Phys. Chem. C*, vol. 2, no. 110,

pp. 8278–8282, 2007.

[9] F. M. Pesci, G. Wang, D. R. Klug, Y. Li, and A. J. Cowan, "Efficient Suppression of Electron − Hole Recombination in Oxygen- Deficient Hydrogen-Treated TiO2 Nanowires for Photoelectrochemical Water Splitting," *J. Phys. Chem. C*, vol. 117, p. 25837, 2013.

[10] J. Dong *et al.*, "Defective black TiO_2 synthesized via anodization for visible-light photocatalysis," *ACS Appl. Mater. Interfaces*, vol. 6, no. 3, pp. 1385–1388, 2014.

[11] X. Jiang *et al.*, "Characterization of Oxygen Vacancies Associates within the Hydrogenated TiO2 : a Positron Annihilation Study Characterization of Oxygen Vacancies Associates within the Hydrogenated TiO_2 : a Positron Annihilation Study," *J.Phys.Chem.C*, vol. 116, pp. 22619–22624, 2012.

[12] L. R. Grabstanowicz *et al.*, "Facile oxidative conversion of TiH_2 to high-concentration Ti3+-self-doped rutile TiO_2 with visible-light photoactivity," *Inorg. Chem.*, vol. 52, no. 7, pp. 3884–3890, 2013.

[13] H. Yin *et al.*, "Gray TiO_2 nanowires synthesized by aluminum-mediated reduction and their excellent photocatalytic activity for water cleaning," *Chem. - A Eur. J.*, vol. 19, no. 40, pp. 13313–13316, 2013.

[14] T. L. Thompson and J. T. Yates, "Surface science studies of the photoactivation of TiO[dw]2[/dw] -- new photochemical processes," *Chem. Rev.*, vol. 106, no. 412, pp. 4428–4453, 2006.

[15] M. M. Khan *et al.*, "Band gap engineered TiO_2 nanoparticles for visible light induced photoelectrochemical and photocatalytic studies," *J. Mater. Chem. A*, vol. 2, no. 3, pp. 637–

644, 2014.

[16] E. Hendry, F. Wang, J. Shan, T. F. Heinz, and M. Bonn, "Electron transport in TiO_2 probed by THz time-domain spectroscopy," *Phys. Rev. B*, vol. 69, no. 8, p. 81101, 2004.

[17] O. K. Varghese, D. Gong, M. Paulose, C. a. Grimes, and E. C. Dickey, "Crystallization and high-temperature structural stability of titanium oxide nanotube arrays," *J. Mater. Res.*, vol. 18, no. 1, pp. 156–165, 2003.

[18] F. Hardcastle, "Raman Spectroscopy of Titania (TiO_2) Nanotubular Water-Splitting Catalysts," *J. Ark. Acad. Sci.*, vol. 65, pp. 43–48, 2011.

[19] T. Bak, J. Nowotny, M. Rekas, and C. C. Sorrell, "Defect chemistry and semiconducting properties of titanium dioxide: II. Defect diagrams," *J. Phys. Chem. Solids*, vol. 64, no. 7, pp. 1057–1067, 2003.

[20] N. Allam and M. El-Sayed, "Photoelectrochemical water oxidation characteristics of anodically fabricated TiO2 nanotube arrays: structural and optical properties," *J. Phys. Chem. C*, vol. 114, pp. 12024–12029, 2010.

[21] Y. Wang, L. Zhang, K. Deng, X. Chen, and Z. Zou, "Low Temperature Synthesis and Photocatalytic Activity of Rutile TiO_2 Nanorod Superstructures," *J. Phys. Chem. C*, vol. 111, no. October, pp. 2709–2714, 2007.

[22] A. W. Amer, M. A. El-Sayed, and N. K. Allam, "Tuning the Photoactivity of Zirconia Nanotubes-Based Photoanodes via Ultrathin Layers of ZrN: An Effective Approach toward Visible-Light Water Splitting," *J. Phys. Chem. C*, vol. 120, no. 13, pp. 7025–7032, 2016.

[23] A. M. Mohamed, A. W. Amer, S. Y. AlQaradawi, and N. K. Allam, "On the nature of defect

states in tungstate nanoflake arrays as promising photoanodes in solar fuel cells," *Phys. Chem. Chem. Phys.*, vol. 18, no. 32, pp. 22217–22223, 2016.

[24] A. Naldoni *et al.*, "Effect of nature and location of defects on bandgap narrowing in black TiO_2 nanoparticles," *J. Am. Chem. Soc.*, vol. 134, no. 18, pp. 7600–7603, 2012.

[25] L. Liu, P. Y. Yu, X. Chen, S. S. Mao, and D. Z. Shen, "Hydrogenation and disorder in engineered black TiO_2," *Phys. Rev. Lett.*, vol. 111, no. 6, pp. 1–5, 2013.

[26] X. Chen, L. Liu, P. Y. Yu, and S. S. Mao, "Increasing solar absorption for photocatalysis with black hydrogenated titanium dioxide nanocrystals.," *Science*, vol. 331, no. 6018, pp. 746–50, 2011.

[27] X. Chen *et al.*, "Properties of disorder-engineered black titanium dioxide nanoparticles through hydrogenation.," *Sci. Rep.*, vol. 3, pp. 1510-1-1510–7, 2013.

[28] Y. H. Hu, "A highly efficient photocatalyst-hydrogenated black TiO2 for the photocatalytic splitting of water," *Angew. Chemie - Int. Ed.*, vol. 51, no. 50, pp. 12410–12412, 2012.

[29] D. C. Hurum, a G. Agrios, K. a Gray, T. Rajh, and M. C. Thurnauer, "Explaining the enhanced photocatalytic activity of Degussa P25 mixed-phase TiO_2 using EPR," *J. Phys. Chem. B*, vol. 107, no. 19, pp. 4545–4549, 2003.

CONCLUSIONS

The hydrogenation of TiO_2 nanostructures was optimized by varying the hydrogen flow rate during the annealing process. XPS analysis showed that changing the flow rate resulted in the formation of different stoichiometric oxides. Raman and UV-Vis spectroscopy analyses were used to study the effect of the anatase-to-rutile ratio on the optical and structural properties of the material. The electrochemical analysis revealed how the anatase-to-rutile ratio affected the concentration of defects and donor density of the samples annealed in different atmospheres and at different flow rates. The low flow rate was found to be insufficient to promote rutile phase formation but could induce deeper trap states and higher density of donor states. On the other hand, high flow rate induced rutile transformation, which decreased the density of deep trap states. Finally, we concluded that there exists an optimum reduction rate that utilizes the high donor density, with relatively low concentration of deep traps and rutile content, to achieve the highest photoconversion efficiency.

Future Work

- **Thin Nanotubes**

Our work involved the use of optimized short tubular structures which can help to deliver more electrons to the metal contact as a result of photo-excitation resulting in higher collection efficiency of electrons. However, the wall thickness of the tubes is still uncontrolled. It is of great importance to reduce the wall thickness of the nanotubes since the hole diffusion length is the bottle neck of the charge transport. Thus, controlling the water content in the anodization process has proven to control the tube diameter and its wall thickness.

- **Metal Doped Hydrogenated TiO_2**

Adding to that, pure TiO_2 got reduced to increase its solar absorption efficiency by hydrogenation. However, doped TiO_2 has shown improved charge transport properties over pure one as well as reduced band gap. It is of great importance to try to hydrogenate metal doped TiO_2 such as Cu, Fe, Wn doped TiO_2. Such process may increase the carrier concentration inside the bulk allowing higher water splitting reaction rate.

Publication

Moamen M. Soliman, Mohamed H. Al Haron, Menna Samir, Basamat S. Shaheen, Ahmed W. Amer, Sarah A. Tolba, Omar F. Mohammed, Nageh K. Allam, Tunable nature of defect states in black TiO_2 nanostructures, Submitted.